Master thesis on Computational Neuroscience
Master of Brain and Cognition
Universitat Pompeu Fabra

A New Modeling Framework for Laminar Neuronal Activity

Roser Sanchez-Todo

Supervisor: Gustavo Deco
Co-Supervisor: Giulio Ruffini

August 2020

Contents

Dedication

Life is a mysterious stream of causal events. I, together with my mentor Giulio Ruffini, would like to dedicate this work to Fabrice Wendling. Because of Fabrice's work on neural mass modeling, Giulio started working on computational modeling some years ago. That relationship evolved into a deep friendship. This in turn led to the creation of a hybrid modeling department at Neuroelectrics, and my eventual hiring to help spearhead its development. These deep scientific and human links, which themselves were preceded by the friendship between Fabrice and Fernando Lopes da Silva (d. 2019), are what have led me to do research with NMMs and write the present thesis.

Acknowledgement

Once more I have the chance to express my sincere gratitude to Giulio (and more times are to come!). Even If I thank him almost daily, I want to dedicate this section to him. Giulio is the coolest mentor and boss one could ever imagine, and I cannot express how lucky I feel to be part of his crew. He is a restless original mind, always bringing up new challenges and opening doors to new adventures. He has a **big heart** and makes people around him grow to be better scientists and, more importantly, **better persons**.

Thanks to him, this thesis has been super **fun** to do, and I have **learned** so much! I hope the reader can feel it when reading through its pages.

Thanks, Giulio! I am looking forward for the next adventure together.

I'd also like to thank Gustavo Deco for his guidance and support through my research in all these years. I am looking forward to the next chapters in our collaboration and his kind mentorship.

Additionally, I'd like to thank Ricardo Salvador and Manel Vila-Vidal for the useful comments and corrections made in the thesis. They helped gain consistency and robustness, and made this work gain another level of perfection. Thanks for all your time, it is very much appreciated.

Abstract

Brain function emerges from interactions between multi-scale networks that can be modeled as a set of interconnected neural mass models (NMM). While biologically inspired, these models cannot directly reproduce the physics of laminar electrophysiology since they are not embedded in a 3D space. Here we present a novel modeling framework to properly simulate multi-laminar recordings by adding a physical layer to a generic version of a NMM, what we call LaNMM. Using this formalism, we propose a specific model architecture able to represent fast (gamma) and slow (alpha) oscillations of laminar recordings and show it can reproduce experimental findings such as depth-frequency distribution, cross-frequency phase and amplitude coupling. While most of the experimental findings are based on LFP data, susceptible to volume conduction artifacts, we also analyse multi-laminar recordings of the prefrontal cortex of macaque monkeys in order to extract more local measurements such as bipolar-LFP (nE) and current source density (CSD), and use them to fit the model parameters with the depth power profiles. We first observe that even if the dynamical parameters of the model are kept fixed, the dynamics of physical quantities, including power profiles of LFP/nE/CSD, are highly sensitive to the choice of synapse locations. Beyond our specific application with LFP multi-probe measurements in a macaque model, this physically realistic modeling framework can be helpful to understand the neural mechanisms behind the origin of oscillation generators in the brain and shed some light into the controversial measuring issues of LFPs, bipolar-LFPs and CSD as well as provide a better model for the coupling of NMM dynamics with EEG/MEG recordings.

Keywords: Laminar Neural Mass Model, Local Field Potential, Relative Power, Laminar Recordings

Chapter 1

Introduction

1.1 Background and motivation

Brain function is the result of interactions between specialized, spatially-segregated areas of brain networks [1]. For this reason, the brain can be modeled as a complex and dynamic multi-scale network to explore the relationship between function and the underlying structure (for a review see [2, 3]). In an earlier study [4], we proposed to represent the human brain as a network of biologically realistic neural mass models (NMM), fitting model parameters with subject-specific structural (MRI, DTI) and functional (EEG) data.

As a starting point, in that first study we relied on Jansen and Rit's NMM [5] to describe cortical column dynamics, with important limitations. On the one hand, this model can represent oscillations only in one specific band for each parameter configuration. This can be a limitation when modeling disorders such as Alzheimer's disease, where there are multifrequency alterations [6]. This can be remedied as in [7], but at the cost of considerably increasing the complexity of the model. On the other hand, neural mass models do not *per se* reproduce the physics of laminar measurements such as Local Field Potentials (LFP) or Current Source Density (CSD), since they are not embedded in a physical 3D space. They do however provide a handle on synaptic current sources and membrane potential, where physics modeling can begin. Physics modeling is necessary to properly contrast model outputs with real electrophysiological recordings, including LFPs, or, further down the line, EEG or MEG data.

There exist computational studies in the literature where NMM parameters are estimated from rodent MUA, LFP and CSD data [8, 9, 10, 11]. The approach taken in these papers to simulate the laminar electrophysiological recordings is to sum the average membrane potential of the populations of each layer as proxy for CSD [8] or to use simpler models and directly extract the average membrane potential or firing rates of the pyramidal populations as the represented MUA [9], LPF [11] or CSD [10] measurements. Other whole-brain computational models used the same approach to relate with more macroscopic electrophysiological recordings (e.g., EEG) in humans [12, 13, 14]. Yet, all these modeling approaches do not represent the NMM in space, thus failing to realistically extract the laminar physics unlike other detailed compartment models [15, 16].

The **first objective** of this thesis is to create a framework to model the cortical column physics by embedding our NMM (Appendix B.2) in a physical matrix. In this framework, we can assign coordinates in space (vertical axis) of apical and basal dendrites of the pyramidal populations and therefore, the locations of each input synapse, which produce a flow of ions across the membrane (a synaptic current). Then, using Poisson equation (the equation that governs the distribution of electrostatic potential in biological media), we can extract the voltage profiles (LFP), the normal component of the field (nE, or bipolar LFP) and CSD. We call this framework *laminar neural mass modelling*, or LaNMM.

In order to model cortical circuitry dynamics, we derive a LaNMM model adapted to simulate multi-laminar LFP recordings of the prefrontal cortex (PFC) of two macaque monkeys doing a working memory task, which will be called McLaNMM. This dataset comes from previous experimental work by A. Bastos and colleagues [17]. In that study, the main findings were that 1) LFP power was strongest in the gamma band (30-250 Hz) for superficial layers and in the alpha/beta band for deep layers and that 2) there was a positive modulation index and a negative Amplitude-Amplitude Coupling (AAC) from deep alpha to superficial gamma oscillations, as well as a causal drive from deep to superficial alpha band (estimated with Granger Causality, GC).

The findings by Bastos et al. were in alignment with other studies where multi-laminar data from the visual cortex of non-human primates were recorded [18, 19, 20, 21, 22, 23, 24]. Nonetheless, there are some experimental discrepancies in these studies regarding the recording site (e.g., not visual cortex) and the type of measurement. Bollimunta et al. [25], using bipolar-LFP and CSD measurements, found alpha in superficial layers for all areas, but only in deep layers for the visual cortices, and a drive from superficial to deep layers of alpha in IT (GC). Ninomyia et al. (2015) [26], also using bipolar-LFP and CSD measurements, could replicate the findings in V1 but not in SEF. Finally, Haegens et al. [27] found an increase of alpha power in deep layers with LFP, but a shift towards superficial layers using CSD measurements (see Appendix A for a literature review table with different animals, recording areas, tasks and measurement type).

A possible explanation for these discrepancies is that LFPs are recorded with respect to a distant reference point and they represent the spatial line integral of the electric field ($\Delta V = -\int_a^b E \cdot dl$), thus susceptible to volume conduction of currents originating from other near or remote sites and common reference noise, which can affect the power distribution and the coupling measurements (e.g. GC). Ultimately, it would be desirable to avoid referencing and/or volume conduction issues by computing either the local normal electric field (approximated as the first spatial derivative of the voltage along the linear array, which removes the referencing issue but not volume conduction confounds) or the CSD (approximated as the second spatial derivative of the voltage multiplied by the tissue conductivity, which takes care of both problems). CSD analysis reveals the location, direction (inwards or outwards) and strength of the flow of ions, and is widely used to distinguish the laminar location of recording sites [28, 17, 29].

In relation to this, the **second objective** of this work is to try to shed some light into these issues by estimating the power profile distribution across the laminae of PFC in macaque monkeys by computing bipolar-LFP (nE) and CSD from the available multi-laminar data [17], together with the exploration of the different coupling schemes between the generators of oscillatory activity.

Based on the initial LFP findings [17], the first version of the model, which we will refer to as McLaNMM, since it simulates laminar physics of macaque depth recordings, is composed of a population of neurons in superficial layers oscillating in gamma and a population of neurons in deep layers oscillating in alpha. We have added a connection from deep to superficial layers in order to simulate the drive from deep alpha to superficial gamma rhythms and other coupling metrics such as MI and AAC. Finally, we derive the second version of the model by fitting the parameters (synapse locations) with the preprocessed data (LFP, nE and CSD) to provide a mechanistic understanding of the distribution of the oscillation generators across the laminae of PFC in macaque monkeys.

1.2 Objectives

To sum up, the main objectives of this study are: 1) extend the NMM formalism to properly simulate LFP, bipolar-LFP (nE) and CSD measurements and 2) process collected LFP data to extract bipolar-LFP and CSD measurements to then fit our model parameters.

1.3 Structure of the Report

This thesis is structured as follows. In the Materials and Methods section, we describe the multi-laminar dataset and its preprocessing, the models used in this study (Synapse-driven NMM) and the extension of the NMM formalism to properly represent laminar physics (LaNMM). Next, we propose a specific LaNMM model to fit the macaque data (McLaNMM). In the Results section, we first try to replicate the results obtained in [17] with our dataset and study the influence of the reference contact on the relative power profiles, complementing it with bipolar-LFP and CSD power profiles. Then, with the first version of the model proposed in the Materials and Methods we try to replicate the LFP-based findings in [17]. Finally, we provide an updated model that replicates the power profiles of LFP, nE and CSD measurements.

Chapter 2

Materials and Methods

In this section, we first describe the multi-laminar LFP recordings from macaque monkeys. This data is from the same experimental dataset as in [17] but involves different animals. Then, we describe the Synapse-driven NMM, a useful reformulation of the work done by Lopes Da Silva and van Rotterdam in the 70s [30, 31, 32], later used in models such as Jansen and Rit [5] or Wendling [33]. This reformulation is done to generalize the equations and be more flexible to create different column architectures. Next, we define the model architecture in order to represent alpha oscillations driving gamma oscillations, which is a combination of two well-known mass configurations, Jansen and Rit [5] and PING [34, 35]. Finally, we develop the physical elements of the model to be added to a general NMM in what we call the LaNMM formalism (Laminar NMM). This allows us to place the neuronal dynamics in space to implement electromagnetic features and compare model outputs with LFP data [17]. The specific model in this study —with parameters optimized to fit multi-laminar LFP data from macaques— is what we call McLaNMM. In Appendix E we provide a summary table of the symbols used in the next sections.

2.1 Multi-laminar recordings

LFPs from the prefrontal cortex (VLPFC, 46dv, 8A) of two macaque monkeys (*Macaca mulatta*) were recorded using a linear array of multi-laminar probes (16 contact, U and V, Plexon) while the animals were performing a working memory task, as described in [17]. For this study, we selected the delay period of the task, and the transition between superficial and deep layers was defined by a visual evoked CSD analysis of the LFPs, where the earliest reliable current sink was used as the zero point to align all the trials and sessions. We removed the contacts belonging to the CSF as in [17], ending up with an average of 11 contacts per session. The reference (ground) of the LFP recordings was on the PFC chamber. We also extracted the first spatial derivative of the voltage along the linear array (nE, bipolar-LFP) and, in order to minimize volume conduction and common noise confounds we computed the second spatial derivative multiplied by the conductivity of the gray matter (CSD).

2.2 Synapse-driven NMM

Neural mass models (NMM) are essentially mathematical abstractions of the dynamics of the average membrane potential and firing rates of a population of neurons in a cortical column [36]. In essence, a second order differential equation describes the currents in each of the synapses that a neuronal population m receives from another one, n. A synapse represents the conversion from an input pre-synaptic firing rate (φ_n) to a membrane potential alteration of the membrane potential ($u_{m\leftarrow n}$) of the post-synaptic neuron, which we represent with the linear operator $L^{-1}_{m\leftarrow n}$ (a linear temporal filter),

$$\begin{aligned} u_{m\leftarrow n}(t) &= L^{-1}_{m\leftarrow n}\big(C_{m\leftarrow n}\,\varphi_n(t)\big) \\ L_{m\leftarrow n}\big(u_{m\leftarrow n}(t)\big) &= C_{m\leftarrow n}\,\varphi_n(t) \end{aligned} \tag{2.1}$$

where $C_{m\leftarrow n}$ is the connectivity constant between the populations. Note that, for simplicity, we use the index notation s to represent the connection/synapse from one neuronal population to another, such that $s \equiv \{m \leftarrow n\colon\ C_{m\leftarrow n} \neq 0\}$. Then the linear operator that describes the synapse dynamics is defined as

$$L_s\big(u_s(t)\big) = \frac{1}{A_s}\left(\tau_s\frac{d^2}{dt^2} + 2\frac{d}{dt} + \frac{1}{\tau_s}\right)u_s(t) \tag{2.2}$$

where A_s is the average excitatory/inhibitory synaptic gain and τ_s the synaptic time constant.

In turn, the post-synaptic neuronal population sums the membrane perturbation from each of the synapses or external perturbations (such as an external electric field), converting its membrane potential (v_m) to an output firing rate (φ_m) in a non-linear manner using a sigmoid function,

$$
\begin{aligned}
v_m(t) &= \sum_s u_s(t) \\
\varphi_m(t) &= \sigma_m\big(v_m(t)\big) \\
\sigma_m\big(v_m(t)\big) &= \frac{2\varphi_0}{1 + e^{r(v_0 - v_m(t))}}
\end{aligned}
\tag{2.3}
$$

where φ_0 is half of the maximum firing rate of each neuronal population, v_0 is the value of the potential when the firing rate is φ_0 and r determines the slope of the sigmoid at the central symmetry point (v_0, φ_0). See Table 3 for the standard parameter values of the model equations.

This is what we call a Synapse-driven formulation of a NMM (Fig. 1), and the model equations are derived from the original Jansen and Rit NMM [5]. See Appendix B for the detailed formulation of the model.

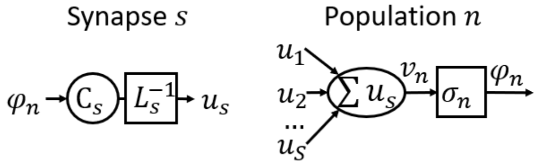

Figure 1: Diagram of the two fundamental components of the synapse-driven formalism. Each synapse s is represented by the linear operator L_s^{-1}. A neuronal population n is represented by the summation of all the pre-synaptic membrane perturbations u_s, and by the non-linear transformation σ_n of its membrane potential v_n into its firing rate φ_n.

2.3 Model architecture

In order to generate the dynamics found in previous studies [17, 20, 19, 21, 26, 37, 24], which found alpha oscillations driving gamma activity, we have combined two well known computational models. Slow oscillations are represented by the Jansen and Rit NMM [5], and the fast ones by the PING model [34, 35], described in Appendix B.2 and Appendix C, respectively.

The Jansen-Rit model (Fig.2A and B, layers IV and V/VI) is composed by a population of pyramidal neurons, P, a population of excitatory cells (interneurons or other pyramidal populations in layer IV), E, and a population representing slow inhibitory interneurons, I (e.g. somatostatin expressing cells). PING (Fig.2A and B, layers II/III) is composed of two populations: a pyramidal population, P', and fast oscillatory interneuron population, I' (e.g. parvalbumin+ basket cells). The connectivity between these models is directed from slow to fast

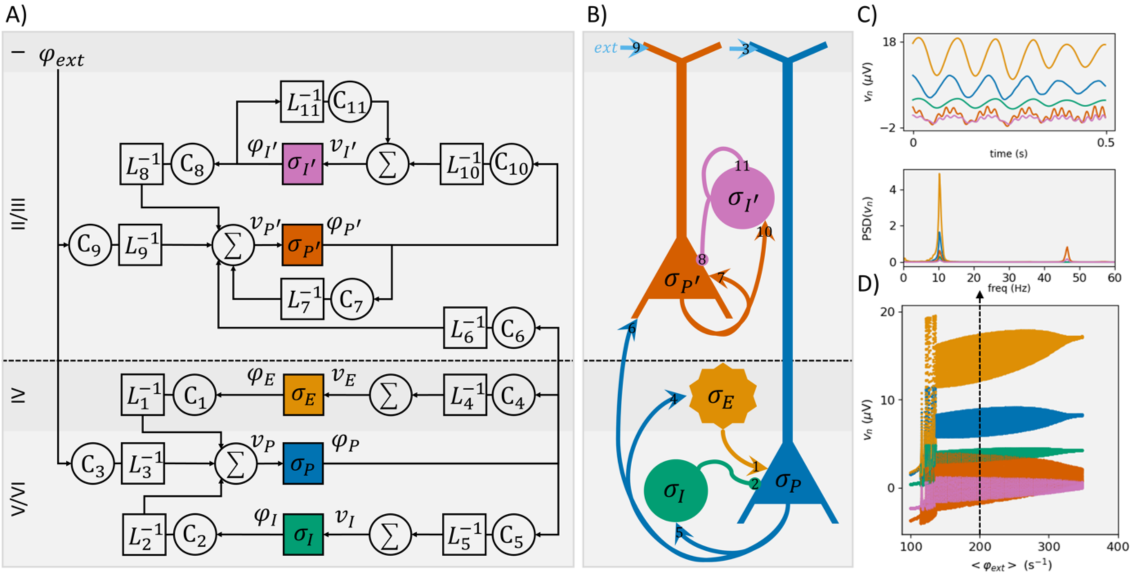

Figure 2: A) Diagram of the model equations. B) Illustration of the neuronal populations with synapse location sites (the locations are used in LaNMM, section 2.4). C) Membrane potential, v_n, of each population and its power spectrum with the mean of the external input noise given by $\varphi_{ext} = 200$. D) Bifurcation diagram with respect to the mean of external input, φ_{ext}, modeled as pink noise.

(C_6, Fig. 2), as suggested by experimental data [17, 18, 21, 23, 26, 24]. The geometric/anatomical connectivity in this case is not taken into account at this stage to keep the model as simple as possible, focusing just on the dynamics. Fig.2 C shows the membrane potential of each of the populations (color-coded) and its PSD profile for an external input noise φ_{ext} with a mean of 200 Hz. Fig.2 D is the bifurcation diagram of the model with respect to the mean input noise of φ_{ext} (also color-coded).

The parameters of the model (Fig. 2) are described in Table 1, and the equations, expressed in the synapse-centric formalism in Appendix B, are the following:

$$
\begin{aligned}
&L_1\big(u_1(t)\big) = C_1\varphi_E = c_1\sigma_E(v_E) = C_1\sigma_E\big(u_4(t)\big)\\
&L_2\big(u_2(t)\big) = C_2\varphi_I = C_2\sigma_I(v_I) = C_2\sigma_I\big(u_5(t)\big)\\
&L_3\big(u_3(t)\big) = C_3\varphi_{ext}\\
&L_4\big(u_4(t)\big) = C_4\varphi_P = C_4\sigma_P(v_P) = C_4\sigma_P\big(u_1(t)+u_2(t)+u_3(t)\big)\\
&L_5\big(u_5(t)\big) = C_5\varphi_P = C_5\sigma_P(v_P) = C_5\sigma_P\big(u_1(t)+u_2(t)+u_3(t)\big)\\
&L_6\big(u_6(t)\big) = C_6\varphi_P = C_6\sigma_P(v_P) = C_6\sigma_P\big(u_1(t)+u_2(t)+u_3(t)\big)\\
&L_7\big(u_7(t)\big) = C_7\varphi_{P'} = C_7\sigma_{P'}(v_{P'}) = C_7\sigma_{P'}\big(u_6(t)+u_7(t)+u_8(t)+u_9(t)\big)\\
&L_8\big(u_8(t)\big) = C_8\varphi_{I'} = C_8\sigma_{I'}(v_{I'}) = C_8\sigma_{I'}\big(u_{10}(t)+u_{11}(t)\big)\\
&L_9\big(u_9(t)\big) = C_9\varphi_{ext}\\
&L_{10}\big(u_{10}(t)\big) = C_{10}\varphi_{P'} = C_{10}\sigma_{P'}(v_{P'}) = C_{10}\sigma_{P'}\big(u_6(t)+u_7(t)+u_8(t)+u_9(t)\big)\\
&L_{11}\big(u_{11}(t)\big) = C_{11}\varphi_{I'} = C_{11}\sigma_{I'}(v_{I'}) = C_{11}\sigma_{I'}\big(u_{10}(t)+u_{11}(t)\big)
\end{aligned}
\tag{2.4}
$$

Table 1: Model parameters. The parameters for the deep neural populations are taken from [5], and for the superficial populations from [35]. The only additional parameters defined are the ones associated to synapse $s = 6$, so that deep oscillations modulate the superficial ones.

Synapse s	C_s	A_s (mV)	τ_s (s^{-1})	layer
1	108	3.25	100	5
2	33.75	-22	50	5
3	1	3.25	100	1
4	135	3.25	100	5
5	33.75	3.25	100	5
6	40	18	108	2
7	10	18	108	2
8	560	-30	132	2
9	0.0067	18	100	1
10	40	18	108	2
11	400	-30	132	2

2.4 LaNMM and McLaNMM

By LaNMM we mean here a framework to build specific laminar models that unite the synapse-centric formalism with physics. Here we describe a specific model built using this framework, that we call McLaNMM. The name reflects the fact that we have designed it to match macaque intracortical data.

More specifically, we work with a column of layer width h, cortical width $6h$, and with a uniform conductivity σ. Given their anatomical characteristics (elongated form factor, which enhances the effects of electric field on membrane polarization), organization (horizontal connectivity, homogeneous orientation in cortical patches and temporal synchronicity), cortical pyramidal cell synapses are the main electric current and field generators [38, 39].

The apical and basal dendrites of the pyramidal populations, with locations across the vertical z axis (Fig.3, $z_l \in [1, 6]$) will be the location of the input/output currents of each of the synapses (sinks and sources, respectively). Each synapse perturbation u_s has its own location in space now (z_l) and will produce a flow of ions across the membrane and, therefore, a synaptic current, I_s (Amperes). Moreover, the membrane perturbation generated by an injected current depends on several factors, including cell morphology and membrane conductivity. We represent these factors with a gain factor η_n (A/mV) and write

$$I_s(z_l) = \begin{cases} \eta_n u_s(z_l) & \text{if } z_l \text{ is the location of } s \\ 0 & \text{Otherwise} \end{cases} \tag{2.5}$$

Note that, for simplicity, we have removed the time dimension of the equations.

Each injected current is accompanied by a capacitive return current (charge conservation), generated by charges accumulated in the membrane. In the current version we model this by assuming two isotropic media with conductivities $\sigma_1 = 0.40$ S/m (gray matter) and $\sigma_2 = 1.79$ S/m (CSF) [40] and a common planar boundary (Fig.3A). The potential induced by a set of point current sources in a space with two conductive media separated by a plane is [38]:

$$V(z) = \frac{1}{4\pi\sigma_1} \sum_s \left[\frac{I_s(z_l)}{R_s(z)} + \left(\frac{\sigma_1 - \sigma_2}{\sigma_1 + \sigma_2} \right) \frac{I_s(z_l)}{R_{s'}(z)} \right] \tag{2.6}$$

Here $R_s(z)$ and $R_{s'}(z)$ are the distances from current source and mirror current source to the recording point (z), respectively (Fig.3A). Once the potential is evaluated, the normal component of the electric field can be computed from its gradient. We can estimate the CSD (A/m^3) from the electric potential using

$$\mathrm{CSD}(z) = -\frac{\sigma}{(\delta z)^2} \Big(V(z + \delta z) - 2V(z) + V(z - \delta z) \Big) \tag{2.7}$$

where σ (S/m) is the tissue conductivity ([41, 42]). The values at the boundary layers are not evaluated. We assume, based on previous studies [43], that inputs to apical dendrites (layer location z_a) create a CSD contribution at the basal dendrites at two locations (layer z_b and z_{b+1}) with half contribution to each, since there are more dendritic ramifications at the soma of the pyramidal neuron (Fig.3B). On the other hand, inputs to the basal dendrites (z_b) create a return also on the layer above (z_{b+1}). That is,

$$
\begin{aligned}
\mathrm{CSD}(z_a) &= \sum_s I_s(z_a) \\
\mathrm{CSD}(z_b) &= \sum_s I_s(z_b) - \frac{1}{2}\sum_s I_s(z_a) \\
\mathrm{CSD}(z_{b+1}) &= -\sum_s I_s(z_b) - \frac{1}{2}\sum_s I_s(z_a)
\end{aligned}
\tag{2.8}
$$

with (charge conservation) $\sum_z \mathrm{CSD}(z) = 0$.

In Fig.3C-E we can observe the different measurements that we can extract from this physical layer of the NMM ($\delta z = 1/72$). The synapse locations are specified in Table 1 and in Fig.2A. We can further extract from this model the dipole current density J, outward normal to the surface, generated by each pyramidal population, which can be used, for example, to predict scalp potential measurements in a rapid manner. Furthermore, this model allows for a realistic representation of the interaction with an external electric field, such as transcranial magnetic or electrical stimulation. For further details, see Appendix D.

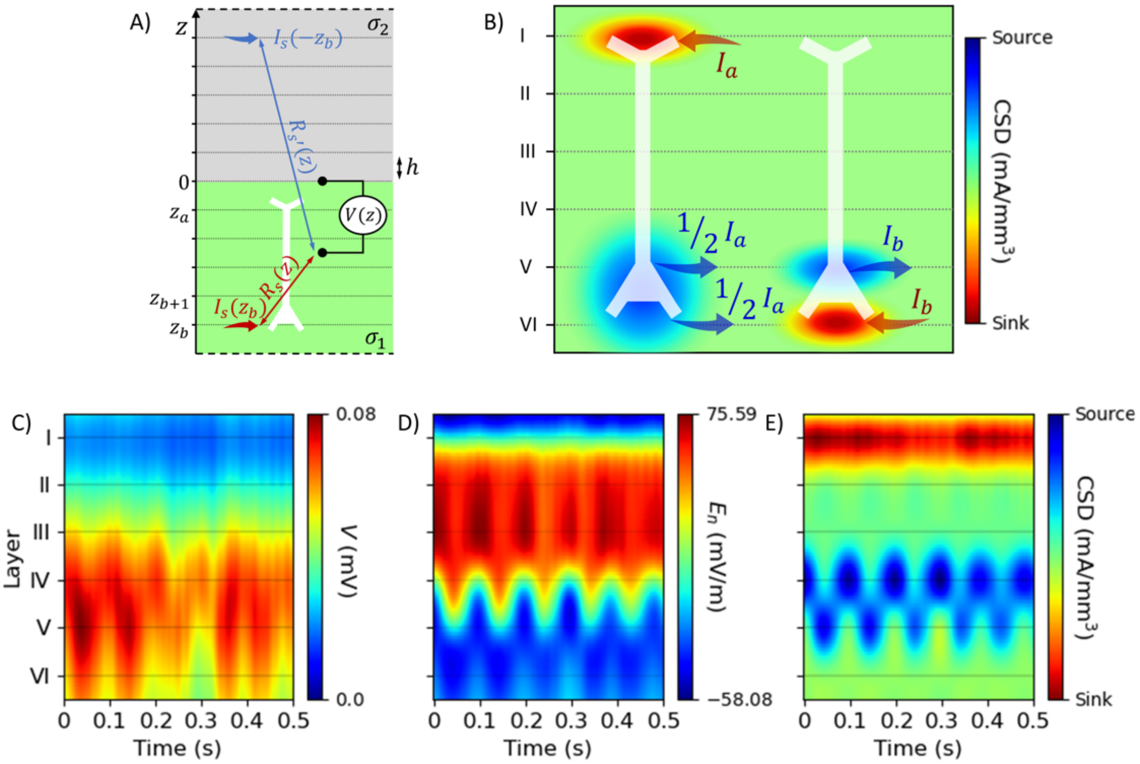

Figure 3: LaNMM and physical features of the McLaNMM. A) Diagram of the equation 2.6. B) Schematic representation of the CSD configuration as in equation 2.8. C) Voltage profile of the McLaNMM taken from equation 2.6. D) What we call the normal component of the electric field (E_n), which is the differential of V across the vertical axis(z). E) The CSD as computed in Equation 2.7.

2.5 Simulation specifications

The models above have been implemented in Python 3.0. We've developed an in-house code *PyLaNMM 1.0* as part of Neuroelectrics' Turing library for hybrid brain modeling [4, 44]. This is a synapse-oriented / object-oriented implementation with hierarchical classes for synapse, neuron, column and cortex, using a fourth order Runge-Kutta solver with a sampling rate of 500 Samples/s. The implementation calls for specification of a sampling frequency, an architecture for the column as well as of external inputs (synaptic and electric field). After the model is run, noise is added (20% of standard deviation of signals) prior evaluation of connectivity metrics.

Chapter 3

Results

3.1 Multi-laminar recordings data analysis

We first used the model to replicate the main results in Bastos et al. (2018) [17] using available data from the same experimental protocol, i.e., processing multi-laminar LFP recordings with the reference in the PFC chamber. The only limitation was that since we didn't have access to data from two adjacent probes in this dataset we could not compute the Granger Causality measures as in [17]. Nonetheless, we focused on replicating 1) the relative voltage power peak on superficial layers in the gamma band and on deep layers in the alpha/beta, 2) the positive modulation index (voltage PAC) and 3) the negative voltage AAC from deep alpha/beta to superficial gamma.

To evaluate the difference in voltage power across each laminar probe, we normalized the power at alpha/beta (4–22 Hz) and gamma (50–250 Hz) frequency bands (as in [17]) and averaged them for all animals, PFC areas, sessions and trials (Fig.4A). The peak gamma power (red line) occurred in superficial layers, 200 μm above the sink, and the peak of alpha/beta power (blue line) occurred in deep layers, -1000 μm below the sink. The intersection point between the profiles occurred between -200 μm and -400 μm, very close to the location of the CSD sink. Hence, gamma power was prominent in superficial layers and alpha/beta power in deep, as in Bastos et al. (2018) [17].

To test whether the phase/amplitude of the slower frequency band coupled with the amplitude of the higher-frequency band, we used phase-amplitude coupling (PAC), amplitude-amplitude coupling (AAC) and Modulation Index (MI). Both PAC and AAC are computed extracting the phase and amplitude of the band-passed signals (in alpha/beta and gamma bands) using the Hilbert transform. The MI is computed as the entropy of the phase-amplitude histogram, with phase measured in the alpha/gamma band and the amplitude in the gamma band. The statistical significance of these values was assessed with a one sample, two-tailed t-test, where the null hypothesis was that the average is not different from zero (*scipy.stats.ttest_ 1samp* in Python).

We found that the influence from superficial alpha/beta phase modulated both superficial and deep gamma amplitude (Fig.4B and C) and that the influence of deep alpha/beta amplitude modulated superficial gamma amplitude (Fig.4D). Nonetheless, most of the AAC values were not significant. These results do not seem to be consistent with the findings of Bastos et al. [17], even though here we used different animals and there could be some unidentified differences in the data-processing.

We then further investigated the effect on these metrics 1) when using a local reference (i.e., the first gray matter contact) instead of the global reference used here (PFC chamber) and 2) when computing the local normal electric field and the CSD (Appendix F).

3.2 Measurement study

To explore the effect of the reference point in the LFP measurements, we have computed the LFP power profile of the same data with different reference points: the PFC chamber (Fig.5A, same as in Fig.4A), the first electrode contact in the gray matter (Fig.5B) and the last (Fig.5C). To complement these results we also evaluated the relative power of the bipolar-LFP (or nE) and CSD measurements (Fig.5D), in order to mitigate the impact of possible far-field sources and referencing artifacts, and get the local current flow.

We observe that the reference point location has a big impact on the LFP power profiles, leading to a peak of the alpha power in superficial layers when the reference is located in the last contact of the probe.

Considering the definition of voltage, $\Delta V = -\int_a^b E \cdot dl$ (where a is the reference location and b the location of the measured point), and the results obtained for bipolar-LFP and CSD measurements, we can see that the alpha and gamma generators could be placed in superficial layers. If we observe the LFP profiles of alpha in Fig.5A,B and C, between contact b_2 and b_6 there is a significant increase in power compared with the power between b_6 and b_{10}, where it

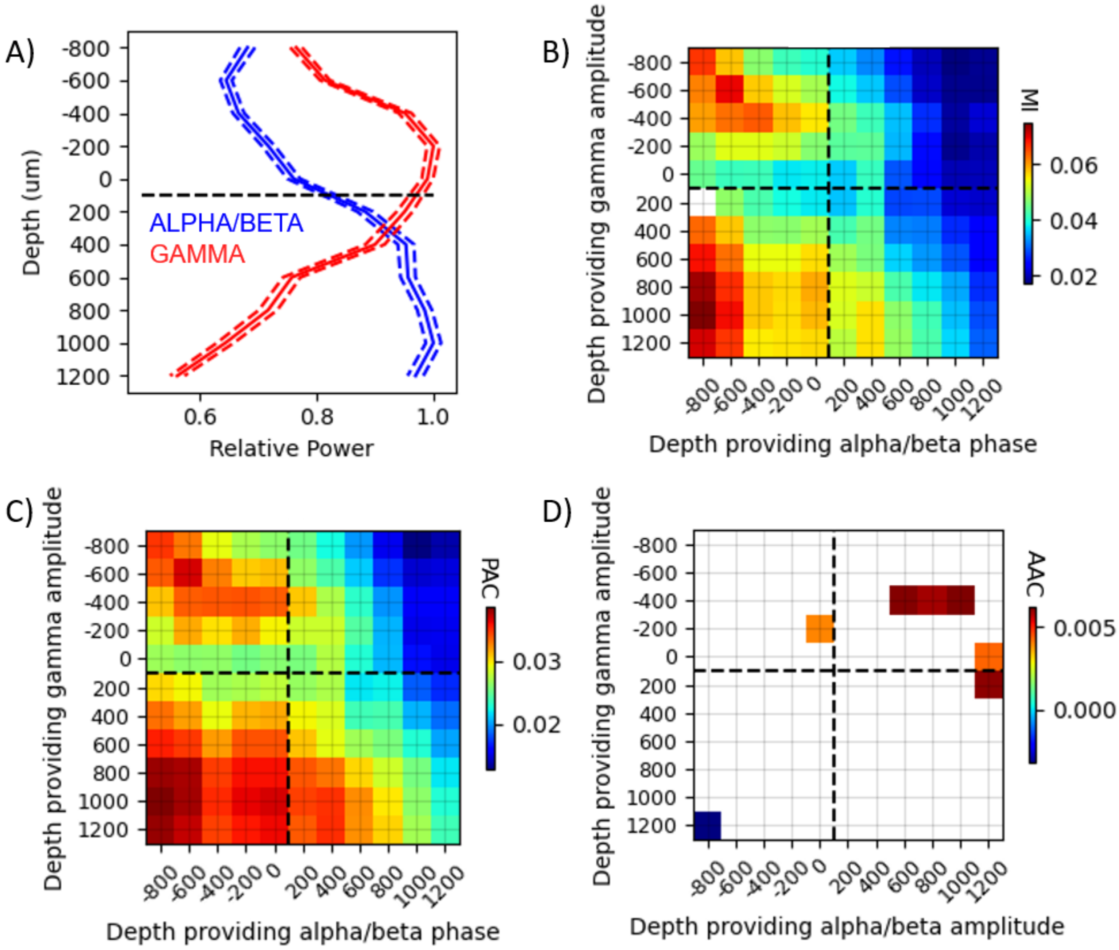

Figure 4: LFP measurements averaged across sessions, trials and animal specimens. A) Normalized power averaged across low (4—22 Hz, blue line) and high (50—250 Hz, red line) frequencies. Error bars ± 2 SEM. B) Modulation Index (MI) and C) Phase-Amplitude Coupling (PAC) between the phase of alpha/beta oscillations and the amplitude of gamma oscillations. D) Amplitude-Amplitude coupling between the amplitude of alpha/beta oscillations and amplitude of gamma oscillations. The dashed black line denotes the transition from superficial to deep layers. White entries represent pairs of contacts that did not show statistically significant measures (p-value$>$0.05, testing the null hypothesis that the average is not different from 0 in a 1 sample, 2-tailed t-test)

plateaus. That means that the spatial integral in the vertical axis sums significant power of alpha between the contacts in superficial layers compared with the ones in deep layers. Moreover, the peak of alpha in nE and CSD measurements occurs in superficial layers as well.

Altogether, we found that both gamma and alpha oscillatory generators could be located in superficial layers, as opposed to what it was previously reported in Bastos et al. (2018) [17].

3.3 Voltage measurements in McLaNMM

We first sought to replicate the same results as in Bastos et al. (2018) [17] with the McLaNMM model (Fig.2). We used the parameters specified in Table 1, with gain factors $\eta_{deep} = 10^{-8}$ for

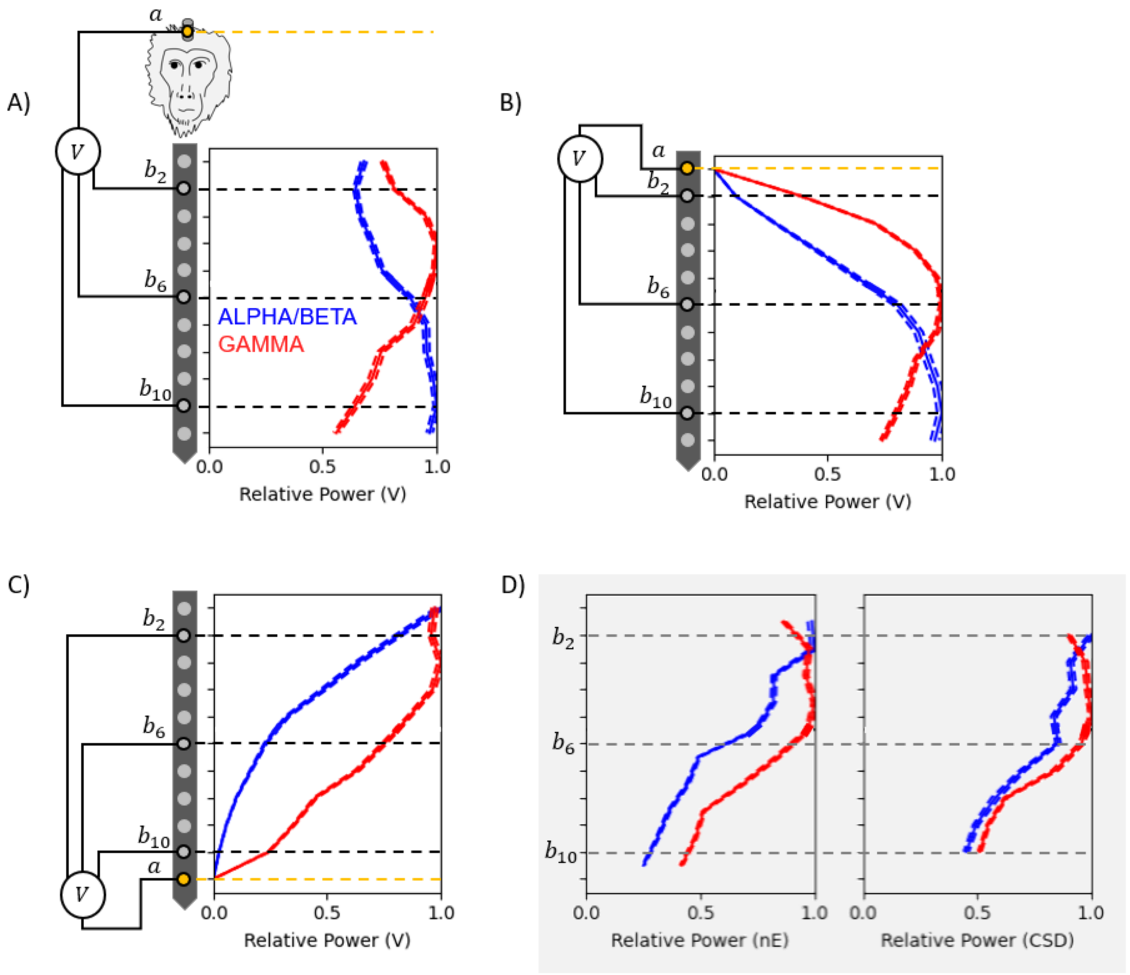

Figure 5: LFP relative power profiles with different reference points, bipolar-LFP and CSD. A) LFP relative power, same as in Fig.4A, with the reference in the PFC chamber. B) Same LFP data re-referenced to the first contact of the gray matter. C) Same LFP data re-referenced to the last contact. D) Bipolar-LFP (nE) and CSD relative power profiles, invariant of the reference point. The yellow contact, a, denotes the reference point, and b_c the different measurements in contacts $c = 2, 6, 10$. The transition between superficial and deep layers happens between the contact 5 and 6.

the deep layer populations and $\eta_{sup} = 10^{-9}$ for the superficial ones, in order to take into account the amount of synapses in each layer and the population morphologies (sampling rate 500 S/s and simulation time 60 s).

Spectral Granger Causality (GC), a measure of statistical prediction between time series [45], was computed using the *spectral_ connectivity* library in Python, for simulated LFPs of two different columns with independent input noise sources (Fig.6A). We found that GC spectrum had peaks in the alpha/beta range, and that directed interactions were asymmetric: deep layer alpha/beta drove superficial layer alpha/beta more than the other way around. These findings are identical to those found in Bastos et al. (2018) [17].

To evaluate the difference in voltage power across layers, we normalized the power of alpha

(8–14 Hz) and gamma (30–50 Hz) frequency bands for one cortical column (Fig.6B). Similar to Bastos et al. (2018) [17], the peak gamma power (red line) occurred in superficial layers and the peak of alpha (blue line) occurred in deep layers.

To test whether the phase/amplitude of the slower frequency band coupled with the amplitude of the higher-frequency band we used the same metrics as in the previous section: MI, PAC, and AAC. We found that the influence of deep alpha phase coupled with superficial gamma amplitude, and that it was stronger from deep to superficial than in the reverse direction (Fig.6C and D). Moreover, deep layer alpha power was negatively correlated with superficial gamma power (Fig.6E).

These findings, even if simplistic, are aligned with the results of Bastos et al. (2018) [17], suggesting that this model can properly simulate the main features of multi-laminar LFP recordings of macaque monkeys.

3.4 Model fit with power profiles

As mentioned in the introduction, we also wanted to explore the model performance in simulating the power profiles for different measurements: LFPs (voltage), bipolar LFPs (normal component of the electric field, nE) and CSD. Since the current model configuration was just to represent the voltage measurements, we have explored different model parameters configurations in order to obtain the desired power profiles (Fig.7A).

The choice of parameters was such that the dynamics of the model didn't change, so we had the same oscillatory activity in the populations, but the physics did. For this reason, we chose just the parameters that influenced the physical measurements: the location of the synapses (Table 1, location) and the synaptic gain η_n.

We explored all possible combinations of such parameters and found that changing the synaptic gain, η_n, we didn't obtain any realistic profile distribution. With the change in the synapse locations we found more realistic profiles. The one that best matched the data is shown in Fig.7B, where we just change the location of the synapse $s = 2$ (Table 1), corresponding to the synapse from the slow inhibitory interneuron to the pyramidal one in deep layers, from location 5 to location 1. This result is consistent with the anatomical circuitry of a column, where the slow interneurons, such as somatostatin expressing cells, synapse to the apical dendrites instead of the basal ones [46, 47, 48].

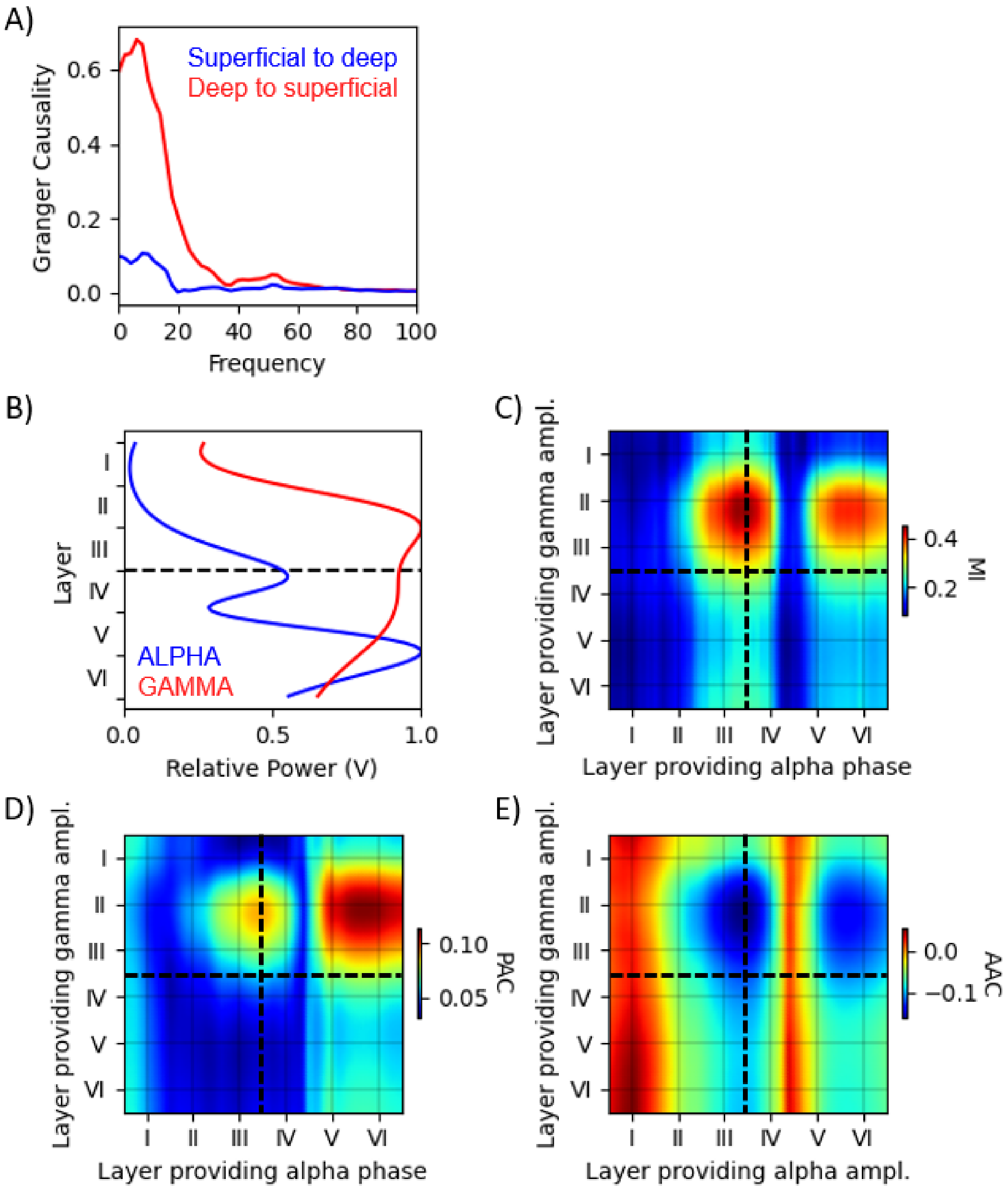

Figure 6: McLaNMM voltage measures. A) Granger Causality (GC) influence across frequencies. The red line represents the GC from deep to superficial layers and the blue line the reverse direction. B) Normalized power across low (8–14 Hz, blue line) and high (30–50 Hz, red line), C) Modulation Index (MI) and D)Phase-Amplitude Coupling (PAC) between the phase of alpha/beta oscillations and the amplitude of gamma oscillations. E) Amplitude-Amplitude coupling between the amplitude of alpha/beta oscillations and amplitude of gamma oscillations. The dashed black line denotes the transition from superficial to deep layers.

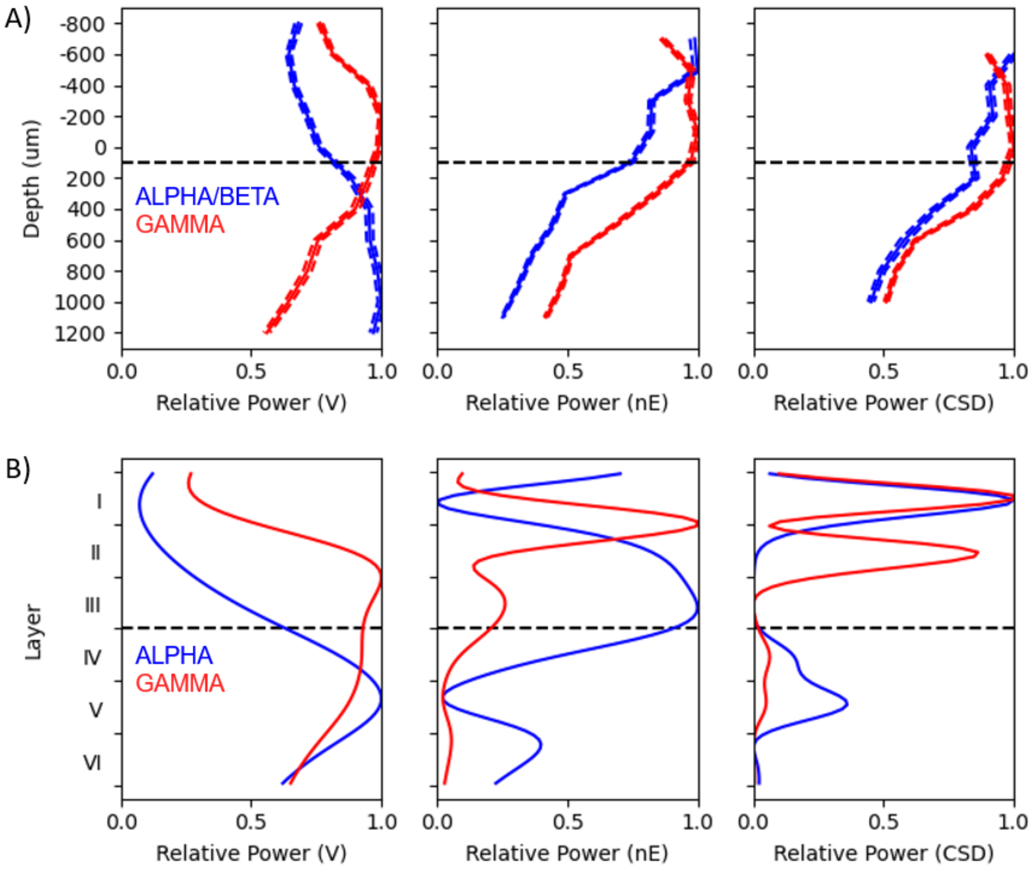

Figure 7: Relative power comparison between macaque multi-laminar data and McLaNMM. A) Grand average of the relative power between monkeys, sessions and trials of the LFPs (V, same as in Fig.4A), nE and CSD, filtered in slow (4—22 Hz, blue line) and high (50—250 Hz,red line) frequency bands. Error bars ± 2 SEM. B) McLaNMM relative power profiles of V, nE and CSD measures filtered in slow (8–14, blue line) and high (30–50Hz, red line) frequency bands. The model parameters are the same as in Table 1, with the exception of the synapse $s = 2$, whose location was in layer 1.

Chapter 4

Discussion and Conclusions

4.1 Discussion

The relative power distribution across layers depends on the choice of the measurement. Figures 5 and 7A show that the distributions of the relative power varies significantly depending on the type of measurement. The distribution of the peak of alpha power shifts to superficial layers when measuring CSD or bipolar-LFPs, in agreement with other existing studies [18, 27]. Altogether, most of the studies that find the peak of alpha in deep layers are based mostly on monopolar LFP recordings, with a remote reference away (on top) from the electrode contacts [17, 20, 19, 49, 23].

The reference issue can be addressed by using bipolar measurements or CSD estimates. Monopolar measurements (LFP) and bipolar-LFPs, unlike CSD measurements, are susceptible to volume conduction from remote sources since they represent the spatial integral of the electric field ($\Delta V = -\int_a^b E \cdot dl$) between two reference points. Therefore, in order to properly interpret LFP measurements, it is important to take into account the slope of the LFP power signal and complement it with more local measurements such as nE, CSD or MUA [25, 18]. Another way to complement the measurements is to re-reference the data to more local electrode contacts, as studied by [26, 23, 27].

A recent study supports our findings regarding the location of alpha sources using micro- and macro-electrodes in epileptic patients, suggesting that alpha is dominated by currents and firing in superficial layers and that it reflects short-range supragranular feedback that propagates from higher- to lower-order cortex and thalamus [50]. Further work employing laminar simultaneous recordings in different brain areas of animal models can shed light to determine if this is consistent across species and tasks.

It is important to note that other factors may influence the power profiles across layers: recording area [27, 26, 25], task type [23, 18, 27, 24], and experimental procedures, such as electrode placement [26]. The proper identification of the transition between superficial and deep layers, which should also depend on the recording site [29, 19, 26], can also be a confound when comparing across studies. Therefore, future work should consider thoughtfully all these factors and not generalize the conclusions to other areas and tasks, while trying to establish a golden standard for the experimental procedures (as suggested by [26]).

Our modeling framework can help shed some light into the generation of cortical rhythms across the laminae. In this study we showed that our modeling framework is able to represent the different oscillatory rhythms across layers and couplings (Fig.6), and the different laminar measurements extracted from multi-contact electrodes (Fig.7) in a physically realistic manner. Moreover, the choice of synapse locations has proven to be a critical element to fit the model to the available data, and has driven the model to a realistic architecture with the slow inhibitory interneuron synapse in layer I.

Limitations. There are several limitations regarding the physical modeling framework we propose in this study (LaNMM). First, when estimating the voltage of the cortical column model (Eq. 2.6), we assume the column can be represented as a single dipole and that the measurement point is relatively far from it. In reality, there is a field of dipoles in the cortical surface/patch and the measurement contact can be placed exactly where the main dipole is located [39]. Other modeling approaches, such as describing the sources as homogeneously distributed in the the horizontal plane, can be explored. Moreover, in our estimation of CSD from data we implicitly assume that all currents occur in a vertical axis, whereas in order to properly extract the CSD we need measurements in 3D space. This assumption could be supported by the fact that pyramidal cells are oriented perpendicular to the surface and they are thought to be the source of cortical dipoles for they elongated shape [39, 38].

Another limitation of this work is that the presented model (McLaNMM) is a relatively simple model, which has just two pyramidal populations located in deep and superficial layers, oscillating in alpha and gamma bands, respectively. This model architecture is inspired by the experimental work of Bastos et al. (2018) [17] and references therein. We didn't explore all possible locations for the pyramidal populations. These were fixed, and then only the synapse locations in their apical or basal dendrites were varied.

As future work, we can explore all range of possibilities: pyramidal cell locations, synapse locations, and even creating new synapses (without changing much the oscillatory dynamics), in order to explore other models proposed in the literature [17, 29, 51, 50]. Furthermore, we could analyze different input schemes (for φ_{ext}), which instead of using pink noise, could represent different oscillatory rhythms as proxy for inputs from other cortical areas or the thalamus [50].

4.2 Conclusions

In this study we extended the NMM formalism (LaNMM) to simulate electrophysiological measurements from laminar multiprobes. We used this framework to simulate and match several features of LFP recordings from macaque data. This was achieved with a specific laminar model: McLaNMM. We fitted model parameters and architecture in order to match the relative power profiles across depth for alpha and gamma oscillatory activity, for different measuring schemes including the LFP itself as well as bipolar-LFP and CSD. This resulted in the McLaNMM architecture —including the specification of synaptic locations, which proved to be an important element. This physically realistic modeling framework will be helpful to understand the neural mechanisms behind the origin of oscillation generators in the brain and shed some light into the controversial issues regarding the measurement of LFPs, bipolar-LFPs and CSD.

Contribution statement

- Conceptualization Ideas: Roser Sanchez-Todo and Giulio Ruffini
- Methodology Development: Roser Sanchez-Todo and Giulio Ruffini
- Software Programming, software development: Roser Sanchez-Todo and Giulio Ruffini
- Investigation Conducting: Roser Sanchez-Todo
- Formal Analysis: Roser Sanchez-Todo and Giulio Ruffini
- Visualization Preparation: Roser Sanchez-Todo
- Writing – Original Draft: Roser Sanchez-Todo
- Mentoring: Gustavo Deco and Giulio Ruffini
- Additional comments: macaque LFP data was collected by André Bastos

List of Figures

List of Tables

Bibliography

[1] Danielle S. Bassett and Olaf Sporns. Network neuroscience. *Nature Neuroscience*, 20(3):353–364, 2017.

[2] Kanika Bansal, Johan Nakuci, and Sarah Feldt Muldoon. Personalized brain network models for assessing structure–function relationships. *Current Opinion in Neurobiology*, 52:42–47, October 2018.

[3] Hannelore Aerts, Wim Fias, Karen Caeyenberghs, and Daniele Marinazzo. Brain networks under attack: Robustness properties and the impact of lesions. *Brain*, 139(12):3063–3083, 2016.

[4] R. Sanchez-Todo, R. Salvador, E. Santarnecchi, F. Wendling, G. Deco, and G. Ruffini. Personalization of hybrid brain models from neuroimaging and electrophysiology data. *BioRxiv*, 2018.

[5] B. H. Jansen and V. G. Rit. Electroencephalogram and visual evoked potential generation in a mathematical model of coupled cortical columns. *Biol Cybern*, 73(4):357–66, 1995.

[6] Jorge J. Palop and Lennart Mucke. Network abnormalities and interneuron dysfunction in Alzheimer disease. *Nature Reviews Neuroscience*, 17(12):777–792, December 2016. Number: 12 Publisher: Nature Publishing Group.

[7] Roberto C. Sotero. Topology, Cross-Frequency, and Same-Frequency Band Interactions Shape the Generation of Phase-Amplitude Coupling in a Neural Mass Model of a Cortical Column. *PLOS Computational Biology*, 12(11):e1005180, November 2016. Publisher: Public Library of Science.

[8] Roberto C. Sotero, Aleksandra Bortel, Ramón Martínez-Cancino, Sujaya Neupane, Peter O'connor, Felix Carbonell, and Amir Shmuel. Anatomically-constrained effective connectivity among layers in a cortical column modeled and estimated from local field potentials.

Journal of Integrative Neuroscience, 09(04):355–379, December 2010. Publisher: Imperial College Press.

[9] Patrick Blomquist, Anna Devor, Ulf G. Indahl, Istvan Ulbert, Gaute T. Einevoll, and Anders M. Dale. Estimation of Thalamocortical and Intracortical Network Models from Joint Thalamic Single-Electrode and Cortical Laminar-Electrode Recordings in the Rat Barrel System. *PLOS Computational Biology*, 5(3):e1000328, March 2009. Publisher: Public Library of Science.

[10] Veronique Lefebvre, Ying Zheng, Chris Martin, Ian M. Devonshire, Samuel Harris, and John E. Mayhew. A Dynamic Causal Model of the Coupling Between Pulse Stimulation and Neural Activity. *Neural Computation*, 21(10):2846–2868, July 2009. Publisher: MIT Press.

[11] R. J. Moran, K. E. Stephan, S. J. Kiebel, N. Rombach, W. T. O'Connor, K. J. Murphy, R. B. Reilly, and K. J. Friston. Bayesian estimation of synaptic physiology from the spectral responses of neural masses. *NeuroImage*, 42(1):272–284, August 2008.

[12] Isabelle Merlet, Gwénaël Birot, Ricardo Salvador, Behnam Molaee-Ardekani, Abeye Mekonnen, Aureli Soria-Frish, Giulio Ruffini, Pedro C. Miranda, and Fabrice Wendling. From Oscillatory Transcranial Current Stimulation to Scalp EEG Changes: A Biophysical and Physiological Modeling Study. *PLoS ONE*, 8(2):1–12, 2013.

[13] Tim Kunze, Alexander Hunold, Jens Haueisen, Viktor Jirsa, and Andreas Spiegler. Transcranial direct current stimulation changes resting state functional connectivity: A large-scale brain network modeling study. *NeuroImage*, 140:174–187, 2016.

[14] Sarah Feldt Muldoon, Fabio Pasqualetti, Shi Gu, Matthew Cieslak, Scott T. Grafton, Jean M. Vettel, and Danielle S. Bassett. Stimulation-Based Control of Dynamic Brain Networks. *PLoS Computational Biology*, 12(9), 2016.

[15] Shane Lee and Stephanie R. Jones. Distinguishing mechanisms of gamma frequency oscillations in human current source signals using a computational model of a laminar neocortical network. *Frontiers in Human Neuroscience*, 7, December 2013.

[16] Espen Hagen, Solveig Næss, Torbjørn V. Ness, and Gaute T. Einevoll. Multimodal Modeling of Neural Network Activity: Computing LFP, ECoG, EEG, and MEG Signals With LFPy 2.0. *Frontiers in Neuroinformatics*, 12, 2018.

[17] André M. Bastos, Roman Loonis, Simon Kornblith, Mikael Lundqvist, and Earl K. Miller. Laminar recordings in frontal cortex suggest distinct layers for maintenance and control of working memory. *Proceedings of the National Academy of Sciences*, 115(5):1117–1122, 2018.

[18] Anil Bollimunta, Jue Mo, Charles E. Schroeder, and Mingzhou Ding. Neuronal mechanisms and attentional modulation of corticothalamic alpha oscillations. *The Journal of Neuroscience: The Official Journal of the Society for Neuroscience*, 31(13):4935–4943, March 2011.

[19] Elizabeth A. Buffalo, Pascal Fries, Rogier Landman, Timothy J. Buschman, and Robert Desimone. Laminar differences in gamma and alpha coherence in the ventral stream. *Proceedings of the National Academy of Sciences of the United States of America*, 108(27):11262–11267, July 2011.

[20] Alexander Maier, Geoffrey K. Adams, Christopher Aura, and David A. Leopold. Distinct superficial and deep laminar domains of activity in the visual cortex during rest and stimulation. *Frontiers in Systems Neuroscience*, 4, 2010.

[21] Eelke Spaak, Mathilde Bonnefond, Alexander Maier, David A. Leopold, and Ole Jensen. Layer-specific entrainment of gamma-band neural activity by the alpha rhythm in monkey visual cortex. *Current biology: CB*, 22(24):2313–2318, December 2012.

[22] Dajun Xing, Chun-I. Yeh, Samuel Burns, and Robert M. Shapley. Laminar analysis of visually evoked activity in the primary visual cortex. *Proceedings of the National Academy of Sciences*, 109(34):13871–13876, August 2012.

[23] Timo van Kerkoerle, Matthew W. Self, Bruno Dagnino, Marie-Alice Gariel-Mathis, Jasper Poort, Chris van der Togt, and Pieter R. Roelfsema. Alpha and gamma oscillations characterize feedback and feedforward processing in monkey visual cortex. *Proceedings of the National Academy of Sciences*, 111(40):14332, October 2014.

[24] Kevin Johnston, Liya Ma, Lauren Schaeffer, and Stefan Everling. Alpha Oscillations Modulate Preparatory Activity in Marmoset Area 8Ad. *Journal of Neuroscience*, 39(10):1855–1866, March 2019.

[25] Anil Bollimunta, Yonghong Chen, Charles E. Schroeder, and Mingzhou Ding. Neuronal mechanisms of cortical alpha oscillations in awake-behaving macaques. *The Journal of*

Neuroscience: The Official Journal of the Society for Neuroscience, 28(40):9976–9988, October 2008.

[26] Taihei Ninomiya, Kacie Dougherty, David C. Godlove, Jeffrey D. Schall, and Alexander Maier. Microcircuitry of agranular frontal cortex: contrasting laminar connectivity between occipital and frontal areas. *Journal of Neurophysiology*, 113(9):3242–3255, May 2015.

[27] Saskia Haegens, Annamaria Barczak, Gabriella Musacchia, Michael L. Lipton, Ashesh D. Mehta, Peter Lakatos, and Charles E. Schroeder. Laminar Profile and Physiology of the alpha Rhythm in Primary Visual, Auditory, and Somatosensory Regions of Neocortex. *The Journal of Neuroscience: The Official Journal of the Society for Neuroscience*, 35(42):14341–14352, October 2015.

[28] N. Maier, V. Nimmrich, and A. Draguhn. Cellular and network mechanisms underlying spontaneous sharp wave-ripple complexes in mouse hippocampal slices. *J Physiol*, 550(Pt 3):873–87, 2003.

[29] David C. Godlove, Alexander Maier, Geoffrey F. Woodman, and Jeffrey D. Schall. Microcircuitry of agranular frontal cortex: testing the generality of the canonical cortical microcircuit. *The Journal of Neuroscience: The Official Journal of the Society for Neuroscience*, 34(15):5355–5369, April 2014.

[30] FH Lopes da Silva, A Hoek, H Smits, and LH (1974) Kyber-netik 15: Zetterberg. Model of brain rhythmic activity: the alpha rhythm of the thalamus. *Kybernetik*, pages 27–37, 1974.

[31] FH Lopes da Silva, van Rotterdam A, P Barts, E Heusden, and W van Burr. Model of neuronal populations: the basic mechanism of rhythmicity. *Prog Brain Res*, 45, 1976.

[32] A van Rotterdam, F H Lopes da Silva, J van den Ende, M A Viergever, and A J Hermans. A model of the spatial-temporal characteristics of the alpha rhythm. *Bulletin of Mathematical Biology*, 44(2):283–305, 1982.

[33] F. Wendling, J. J. Bellanger, F. Bartolomei, and P. Chauvel. Relevance of nonlinear lumped-parameter models in the analysis of depth-EEG epileptic signals. *Biol Cybern*, 83(4):367–378, October 2000.

[34] C. Borgers, S. Epstein, and N. J. Kopell. Gamma oscillations mediate stimulus competition and attentional selection in a cortical network model. *Proceedings of the National Academy of Sciences*, 105(46):18023–18028, November 2008.

[35] Behnam Molaee-Ardekani, Pascal Benquet, Fabrice Bartolomei, and Fabrice Wendling. Computational modeling of high-frequency oscillations at the onset of neocortical partial seizures: from ‘altered structure’ to ‘dysfunction’. *Neuroimage*, 52(3):1109–22, 2010.

[36] F. H. Lopes da Silva, A. van Rotterdam, P. Barts, E. van Heusden, and W. Burr. Models of Neuronal Populations: The Basic Mechanisms of Rhythmicity. In M. A. Corner and D. F. Swaab, editors, *Progress in Brain Research*, volume 45 of *Perspectives in Brain Research*, pages 281–308. Elsevier, January 1976.

[37] J.J. Bonaiuto, S.S. Meyer, S. Little, H. Rossiter, M.F. Callaghan, F. Dick, G.R. Barnes, and S. Bestmann. Lamina-specific cortical dynamics in human visual and sensorimotor cortices. *eLife*, 7(e33977), 2018.

[38] P. L. Nunez and R. Srinivasan. *Electric Fields of the Brain: theNeurophysics of EEG*. Oxford University Press, USA, 2006.

[39] György Buzsáki, Costas A. Anastassiou, and Christof Koch. The origin of extracellular fields and currents — EEG, ECoG, LFP and spikes. *Nature Reviews Neuroscience*, 13:407, 2012.

[40] Pedro Cavaleiro Miranda, Abeye Mekonnen, Ricardo Salvador, and Giulio Ruffini. The electric field in the cortex during transcranial current stimulation. *Neuroimage*, 70:45–58, 2013.

[41] U Mitzdorf. Current source-density method and application in cat cerebral cortex: investigation of evoked potentials and EEG phenomena. *Physiol Rev*, 65(37–100), 1985.

[42] C Quairiaux, P Megevand, J.Z Kiss, and C Michel. Functional Development of Large-Scale Sensorimotor Cortical Networks in the Brain. *The Journal of Neuroscience*, 31(26):9574–9584, 2011.

[43] S Leski, KH Pettersen, B Tunstall, GT Einevoll, and DK Gigg, J DK Wójcik. Inverse current source density method in two dimensions: inferring neural activation from multielectrode recordings. *Neuroinformatics*, 9(4):401–25, December 2011.

[44] Giulio Ruffini, Fabrice Wendling, Roser Sanchez-Todo, and Emiliano Santarnecchi. Targeting brain networks with multichannel transcranial current stimulation (tCS). *Current Opinion in Biomedical Engineering*, 2018.

[45] Adriano B. L. Tort, Robert Komorowski, Howard Eichenbaum, and Nancy Kopell. Measuring Phase-Amplitude Coupling Between Neuronal Oscillations of Different Frequencies. *J Neurophysiol*, 104:1195–1210, 2010.

[46] Henry Markram, Maria Toledo-Rodriguez, Yun Wang, Anirudh Gupta, Gilad Silberberg, and Caizhi Wu. Interneurons of the neocortical inhibitory system. *Nature Reviews Neuroscience*, 5(10):793–807, October 2004. Number: 10 Publisher: Nature Publishing Group.

[47] Robin Tremblay, Soohyun Lee, and Bernardo Rudy. GABAergic Interneurons in the Neocortex: From Cellular Properties to Circuits. *Neuron*, 91(2):260–292, July 2016.

[48] Yves Denoyer, Isabelle Merlet, Fabrice Wendling, and Pascal Benquet. Modelling acute and lasting effects of tDCS on epileptic activity. *Journal of Computational Neuroscience*, 48(2):161–176, May 2020.

[49] Matthew A. Smith, Xiaoxuan Jia, Amin Zandvakili, and Adam Kohn. Laminar dependence of neuronal correlations in visual cortex. *Journal of Neurophysiology*, 109(4):940–947, February 2013.

[50] Milan Halgren, István Ulbert, Hélène Bastuji, Dániel Fabó, Lorand Erőss, Marc Rey, Orrin Devinsky, Werner K. Doyle, Rachel Mak-McCully, Eric Halgren, Lucia Wittner, Patrick Chauvel, Gary Heit, Emad Eskandar, Arnold Mandell, and Sydney S. Cash. The generation and propagation of the human alpha rhythm. *Proceedings of the National Academy of Sciences*, 116(47):23772–23782, November 2019.

[51] Anne-Lise Giraud and David Poeppel. Cortical oscillations and speech processing: emerging computational principles and operations. *Nature Neuroscience*, 15(4):511–517, April 2012.

[52] F. Grimbert and Olivier Faugeras. Analysis of Jansen's model of a single cortical column. *INRIA*, June 2006.

[53] Anita K. Roopun, Steven J. Middleton, Mark O. Cunningham, Fiona E. N. LeBeau, Andrea Bibbig, Miles A. Whittington, and Roger D. Traub. A beta2-frequency (20-30 Hz) oscillation in nonsynaptic networks of somatosensory cortex. *Proceedings of the National Academy of Sciences of the United States of America*, 103(42):15646–15650, October 2006.

[54] Wenzhi Sun and Yang Dan. Layer-specific network oscillation and spatiotemporal receptive field in the visual cortex. *Proceedings of the National Academy of Sciences of the United States of America*, 106(42):17986–17991, October 2009.

[55] Anita K. Roopun, Fiona E.N. LeBeau, James Rammell, Mark O. Cunningham, Roger D. Traub, and Miles A. Whittington. Cholinergic Neuromodulation Controls Directed Temporal Communication in Neocortex in Vitro. *Frontiers in Neural Circuits*, 4, March 2010.

[56] Roberto C. Sotero, Aleksandra Bortel, Shmuel Naaman, Victor M. Mocanu, Pascal Kropf, Martin Y. Villeneuve, and Amir Shmuel. Laminar Distribution of Phase-Amplitude Coupling of Spontaneous Current Sources and Sinks. *Frontiers in Neuroscience*, 9, 2015.

[57] Anirvan S. Nandy, Jonathan J. Nassi, and John H. Reynolds. Laminar Organization of Attentional Modulation in Macaque Visual Area V4. *Neuron*, 93(1):235–246, January 2017.

[58] Milan Halgren, Daniel Fabó, István Ulbert, Joseph R. Madsen, Lorand Erőss, Werner K. Doyle, Orrin Devinsky, Donald Schomer, Sydney S. Cash, and Eric Halgren. Superficial Slow Rhythms Integrate Cortical Processing in Humans. *Scientific Reports*, 8(1):1–12, February 2018.

[59] B. H. Jansen, G. Zouridakis, and M. E. Brandt. A neurophysiologically-based mathematical model of flash visual evoked potentials. *Biol Cybern*, 68(3):275–83, 1993.

[60] Saeed Ahmadizadeh, Philippa J. Karoly, Dragan Nešić, David B. Grayden, Mark J. Cook, Daniel Soudry, and Dean R. Freestone. Bifurcation analysis of two coupled Jansen-Rit neural mass models. *PLOS ONE*, 13(3):1–51, 2018.

[61] Peter Lakatos and et al. Entrainment of neuronal oscillations as a mechanism of attentional selection. *Science*, 320:110–113, April 2008.

[62] Giulio Ruffini, Fabrice Wendling, Isabelle Merlet, Behnam Molaee-Ardekani, Abeye Mekkonen, Ricardo Salvador, Aureli Soria-Frisch, Carles Grau, Stephen Dunne, and Pedro Miranda. Transcranial Current Brain Stimulation (tCS): Models and Technologies. *IEEE Transactions on Neural Systems and Rehabilitation Engineering*, 21(3):333–345, May 2013.

Appendix A

Literature review table

Table 2: Literature Review on layer specific oscillations and couplings (Order by publication date). Abbreviations: Rat in Vitro (RV), Rat (R), Macaques (M), Rhesus Monkeys (RM), Humans (H), Computational Model (CM), Marmoset (Mt), Resting-State (R-S), Visual Evoked Potentials (VEP), Working Memory (WM), Local Field Potential gradients (LFPg), Superficial layers (Sup.), Deep layers (Deep), layer (l), Granger Causality (GC). Red colored text indicates discrepancies in the general findings [17]

Ref.	Animal	Area	Task	Measure	Sup.	Deep	Couplings
Roopun (2006)[53]	RV	A1, S1	-	Cell rec.	γ	$\beta 2$	-
Bollimunta (2008)[25]	M	V2, V4, IT	Sensory	MUA LFP-bipolar CSD	α	α (V2, V4)	GC from Deep α to Sup in V2 and V4 but the opposite for IT.
Sun (2009)[54]	R	V1	R-S and visual	Cell rec.	δ	α	-
Roopun (2010)[55]	RV, CM	A1, P	-	Cell rec.	γ	β	-
Maier (2010)[20]	M	V1	R-S, Visual	LFP	γ	α	Coherence between Sup-Sup and Deep-Deep but not Sup-Deep.
Buffalo (2011)[19]	RM	V1, V2, V4	Visual	MUA, LFP	γ	α	-
Bollimunta (2011)[18]	M	V1	Visual, auditory	LFP, CSD (auditory), MUA	α	α	GC: Deep α drives Sup α
Spaak (2012)[21]	M	V1	R-S	LFP-bipolar CSD	γ	α	+PAC and -AAC from Deep α to Sup γ
Giraud (2012)[51]	H, CM	A1	R-S Speech	SEEG	γ	θ (IV)	PAC from θ in l-IV to Sup γ.
Xing (2012)[22]	M	V1	Visual	MUA LFP	γ	-	-

Smith (2013)[49]	M	V1	Visual	LFP	γ	α	-
van Kerkoerle (2014)[23]	M	V1, V4	Visual	CSD, MUA, LFPs	γ	α	GC: Deep α drives Sup α
Godlove (2014)[29]	M	SEF	Visual	LFP	γ	-	-
Sotero (2015) [56]	R	S1	R-S	CSD	δ, θ, α, β, γ	δ, θ, β, γ	PAC: from θ, α to γ in the same layers (mostly Sup).
Ninomiya (2015)[26]	M	V1, SEF	R-S, VEP	LFP-bipolar	γ	α	+PAC/MI between α phase in Deep and γ amplitude in Sup (V1, not SEF).
Haegens (2015)[27]	M	V1, S1, A1	R-S Sensory Stim.	LFP MUA CSD	α CSD	α LFP	-
Nandy (2017)[57]	M	V1	Attention	LFP	-	β, γ	
Bastos (2018)[17]	M	PFC	WM	LFP MUA	γ	α	GC of α from Deep to Sup., +MI and -AAC from Deep α, β to Sup γ
Halgren (2018)[58]	H	Front. Temp. Par.	R-S vs. Sleep	ECpG, iEEG, LFPg-bipolar, CSD	δ, θ	-	PAC/MI: δ phase modulated θ power. Both δ, θ in Sup. modulated the power of α, β, γ in both states of the rest of the layers, and the power was maximal in the up phase.
Bonaiuto (2018)[37]	H	V1, S1	Visual Attention	MEG	γ	α	-
Johnston (2019)[24]	Mt	8ad, lat-Parietal	Visual	LFP	γ 8ad	α 8ad	-MI of Deep α to Sup. γ.

Appendix B

From Jansen and Rit to a Synapse-driven model

B.1 Jansen and Rit model description

In 1993 Jansen and Rit [59] developed a model of a cortical column which consists of three different neural populations: Pyramidal neurons (P), inhibitory interneurons (I) and excitatory interneurons (E). The state variables of the model are the membrane potential and the firing rate of the neuron populations, and they are linked by two different transformations that shape the classical properties of neurons: the pulse-to-wave, $h(t)$, and wave-to-pulse, $\sigma(v)$ functions [52, 60].

The $\sigma(v)$ operator, also called "wave-to-pulse", introduces a nonlinear component that transforms the average membrane potential of a population, $v(t)$, in mV, into the average firing rate, $\varphi(t)$:

$$\varphi(t) = \sigma\big(v(t)\big) = \frac{2\varphi_0}{1 + e^{r(v_0 - v(t))}} \tag{B.1}$$

where φ_0 is half of the maximum firing rate of each neuronal population, v_0 is the value of the potential when the firing rate is φ_0 and r determines the slope of the sigmoid at the central symmetry point (v_0, φ_0). See Table 3 for the standard parameter values of the model equations.

The $h(t)$ operator, also called "pulse-to-wave", converts the average rate of action potentials into an average post-synaptic potential, either excitatory, $h_{0,1}(t)$, or inhibitory, $h_2(t)$. The

Table 3: Parameters, description and standard values of the JR synapse model. Values taken from [5]

Parameter	Description	Value
A_s	Average excitatory and inhibitory synaptic gain	$A_{1,3,4,5} = 3.25\,mV$ $A_2 = -22.\,mV$
τ_s	Time constant of average excitatory and inhibitory post synaptic potentials	$\tau_{1,3,4,5} = 100\,s^{-1}$ $\tau_2 = 50\,s^{-1}$
C_s	Average number of synaptic contacts between population types	$C_1 = 108.$ $C_2 = 33.7$ $C_3 = 1$ $C_4 = 135.$ $C_5 = 33.75$
v_0	Potential when 50% of the firing rate is achieved	$6\,mV$
φ_0	Half of the maximum firing rate	$2.5\,Hz$
r	Slope of the sigmoid function at v_0	$0.56\,mV^{-1}$

transformation is done through a second order differential linear transform whose equivalent impulse response is given by:

$$h(t) = \begin{cases} \frac{A}{\tau} t e^{-t/\tau} & t \geq 0 \\ 0 & t < 0 \end{cases} \tag{B.2}$$

Each of these post-synaptic boxes corresponds to solving a differential equation such as:

$$\ddot{u}(t) = \frac{A}{\tau}\varphi(t) - \frac{2}{\tau}\dot{u}(t) - \frac{1}{\tau^2}u(t) \tag{B.3}$$

where $\varphi(t)$ is the output of the sigmoid function (average firing rate of a population) as well as the input to the linear function $h(t)$, and $u(t)$ is the membrane potential alteration in each of the synapses. The parameters A and $1/\tau$ represent the maximal amplitude of excitatory or inhibitory post-synaptic potential and the average time constant for each synapse type, respectively.

This second order differential equation can be decomposed in a system of two equations,

$$\begin{aligned} \dot{u}(t) &= z(t) \\ \dot{z}(t) &= \frac{A}{\tau}\varphi(t) - \frac{1}{\tau}2z(t) - \frac{1}{\tau^2}u(t) \end{aligned} \tag{B.4}$$

There are thus three main state variables in the model: the average membrane potential of each of the subpopulations of the system: $v_P(t)$ for the pyramidal cells, and $v_E(t)$, $v_I(t)$ for the

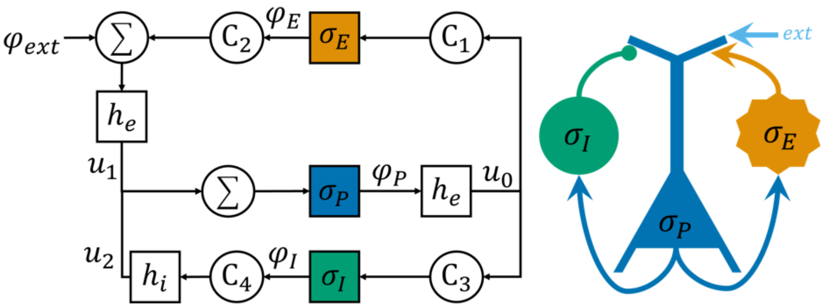

Figure 8: Diagram of Jansen and Rit equations, adapted from [52]

excitatory and inhibitory interneurons, respectively. Here v_P is the main output of the model since the sum of the membrane potentials of the pyramidal neurons has been typically used as a proxy source of electrophysiological signals such as LFPs and EEG (dipole generator). This approximation will be revised by future follow-up work using the LaNMM framework.

The Jansen and Rit model can be described with a set of six differential equations, with each pair corresponding to each of the populations:

$$
\begin{aligned}
\dot{u}_0(t) &= u_3(t) \\
\dot{u}_3(t) &= \frac{A_0}{\tau_0}\Big[\sigma_P\big(u_1(t) - u_2(t)\big)\Big] - 2\frac{1}{\tau_0}u_3(t) - \frac{1}{\tau_0^2}u_0(t) \\
\dot{u}_1(t) &= u_4(t) \\
\dot{u}_4(t) &= \frac{A_1}{\tau_1}\Big[\varphi_{ext}(t) + C_2\sigma_E\big(C_1u_0(t)\big)\Big] - 2\frac{1}{\tau_1}u_4(t) - \frac{1}{\tau_1^2}u_1(t) \\
\dot{u}_2(t) &= u_5(t) \\
\dot{u}_5(t) &= \frac{A_2}{\tau_2}\Big[C_4\sigma_I\big(C_3u_0(t)\big)\Big] - 2\frac{1}{\tau_2}u_5(t) - \frac{1}{\tau_2^2}u_2(t)
\end{aligned}
\tag{B.5}
$$

For an illustrative description of the model equations see Figure 8. In this cortical column configuration the membrane potential of the pyramidal population is $v_P(t) = u_1(t) - u_2(t)$, the membrane potential of the inhibitory interneuron population is $v_I = C_3u_0$ and of the excitatory interneuron population is $v_E = C_1u_0$,

B.2 Derivation of the Synapse-driven model from Jansen and Rit equations

We can rewrite the Jansen and Rit NMM focusing on the dynamics each of the synapses independently, which will allow us to generalize the equations and simplify the definition of the neural dynamics for the development of more complex models. We will define a new linear operator, $L^{-1}(\cdot)$, to transform pre-synaptic average firing rate form neuron n, φ_n, into post-synaptic membrane perturbation of neuron m, $u_{m\leftarrow n}$:

$$\begin{aligned} u_{m\leftarrow n}(t) &= L^{-1}_{m\leftarrow n}\big(C_{m\leftarrow n}\,\varphi_n(t)\big) \\ L_{m\leftarrow n}\big(u_{m\leftarrow n}(t)\big) &= C_{m\leftarrow n}\,\varphi_n(t) \end{aligned} \tag{B.6}$$

$L^{-1}(\cdot)$ is the inverse of the $L(\cdot)$ operator and can be expressed as an integral (convolution) operator using the typical $h(t)$ box function,

$$L^{-1}\big(f(t)\big) = \int_{-\infty}^{\infty} dt'\, h(t-t')f(t')$$

Note that, for simplicity, the index s will represent the connection/synapse from one neuronal population to another $m \leftarrow n$, where $n, m \in [P, E, I, ext]$ and $(m,n)\colon\ C_{m\leftarrow n} \neq 0\}$. Then, we can define the linear operator $L_s(\cdot)$ that represents the synapse dynamics as:

$$L_s\big(u_s(t)\big) = \frac{1}{A_s}\left(\tau_s\frac{d^2}{dt^2} + 2\frac{d}{dt} + \frac{1}{\tau_s}\right)u_s(t) \tag{B.7}$$

The sum of each pre-synaptic perturbation into neuron n is the membrane potential of the post-synaptic neuron, v_m,

$$v_m(t) = \sum_s u_s(t) \tag{B.8}$$

and the average firing rate of the neural population, φ_m, is the output of the non-linear function,

$$\begin{aligned} \varphi_m(t) &= \sigma_m\big(v_m(t)\big) \\ \sigma_m\big(v_m(t)\big) &= \frac{2\varphi_0}{1+e^{r(v_0-v_m(t))}} \end{aligned} \tag{B.9}$$

Within the synapse-driven formalism, the Jansen and Rit equations specify the dynamics as a function of the average firing rate for each neural population φ_n, the average membrane potential for each population v_n and the membrane perturbation per each synapse u_s,

$$\begin{aligned}
L_1\big(u_1(t)\big) &= C_1\varphi_P = C_1\sigma(v_P) = C_1\sigma\big(u_2(t) + u_5(t) + u_4(t)\big) \\
L_2\big(u_2(t)\big) &= C_2\varphi_E = C_2\sigma(v_E) = C_2\sigma\big(u_1(t)\big) \\
L_3\big(u_3(t)\big) &= C_3\varphi_P = C_3\sigma(v_P) = C_3\sigma\big(u_2(t) + u_5(t) + u_4(t)\big) \\
L_4\big(u_4(t)\big) &= C_4\varphi_I = C_4\sigma(v_I) = C_4\sigma\big(u_3(t)\big) \\
L_5\big(u_5(t)\big) &= C_5\varphi_{ext}(t)
\end{aligned} \tag{B.10}$$

The diagram and dynamics of the Jansen and Rit NMM in the Synapse-driven implementation is represented in Figure 9. Fig.9 C shows the membrane potential of each of the populations (color-coded) and its PSD profile for an external input noise φ_{ext} with a mean of 200 Hz. Fig.9 D is the bifurcation diagram of the model with respect to the mean input noise of φ_{ext} (also color-coded).

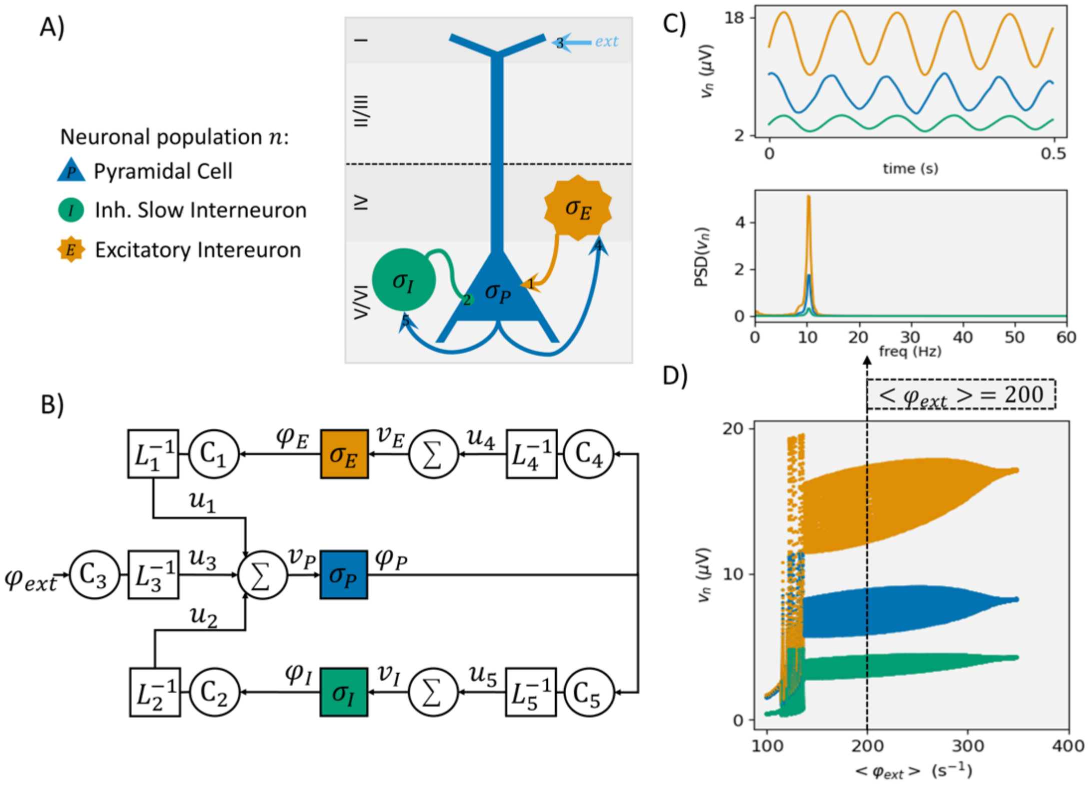

Figure 9: Jansen and Rit Synapse-driven model. A) Illustration of the neuronal populations with synapse location sites. B) Diagram of the model equations. C) Membrane potential, v_n, of each population and its power spectral density with the mean of the external input noise given by $\varphi_{ext} = 200$. D) Bifurcation diagram with respect to the mean of external input, φ_{ext}, modeled as pink noise.

Appendix C

Pyramidal Interneuron Gamma model - PING

The Pyramidal Interneuron Gamma model (PING) involves the combination of a pyramidal population and a fast inhibitory interneuron (e.g. Basket cells). In the synapse driven formalism, the parameters are summarized in table Table 4, and the equations are

$$\begin{aligned}
L_1\big(u_1(t)\big) &= C_1\varphi_P = C_1\sigma(v_P) = C_1\sigma\big(u_1(t)+u_2(t)+u_3(t)\big)\\
L_2\big(u_2(t)\big) &= C_2\varphi_I = C_2\sigma(v_I) = C_2\sigma\big(u_4(t)+u_5(t)\big)\\
L_3\big(u_3(t)\big) &= C_3\varphi_{ext}(t)\\
L_4\big(u_4(t)\big) &= C_4\varphi_P = C_4\sigma(v_P) = C_4\sigma\big(u_1(t)+u_2(t)+u_3(t)\big)\\
L_5\big(u_5(t)\big) &= C_5\varphi_I = C_5\sigma(v_I) = C_5\sigma\big(u_4(t)+u_5(t)\big)
\end{aligned} \tag{C.1}$$

The diagram and dynamics of the PING NMM in the Synapse-driven implementation is represented in Figure 10. Fig.10 C shows the membrane potential of each of the populations (color-coded) and its PSD profile for an external input noise φ_{ext} with a mean of 200 Hz. Fig.10 D is the bifurcation diagram of the model with respect to the mean input noise of φ_{ext} (also color-coded).

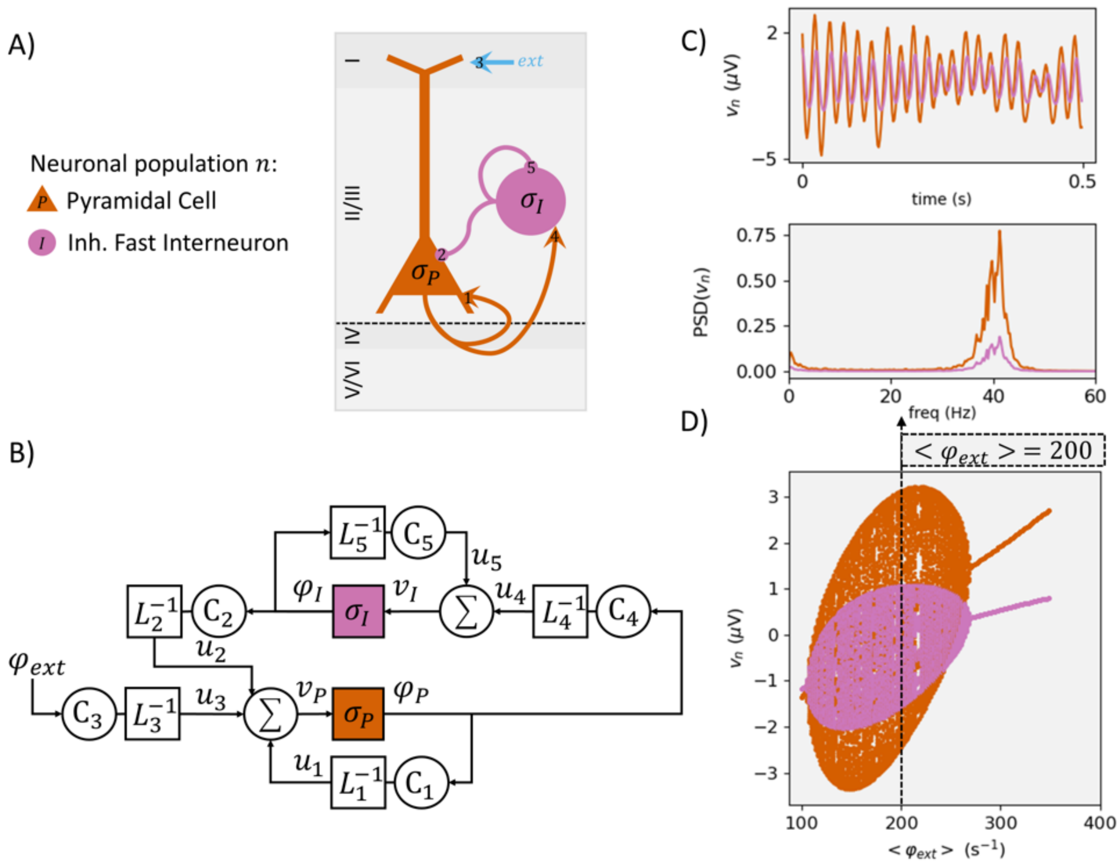

Figure 10: PING Synapse-driven model. A) Illustration of the neuronal populations with synapse location sites. B) Diagram of the model equations. C) Membrane potential, v_n, of each population and its power spectral density with the mean of the external input noise given by $\varphi_{ext} = 200$. D) Bifurcation diagram with respect to the mean of external input, φ_{ext}, modeled as pink noise.

Table 4: Parameters, description and standard values of the PING synapse model. Values taken from [35]. Here, we have modified the τ parameter so the neural mass oscillates in slow gamma instead of fast gamma.

Parameter	Description	Value
A_s	Average excitatory and inhibitory synaptic gain	$A_{1,3,4} = 18\,mV$ $A_{2,5} = 22.\,mV$
τ_s	Time constant of average excitatory and inhibitory post synaptic potentials	$\tau_{1,3,4} = 108\,s^{-1}$ $\tau_{2,5} = 132\,s^{-1}$
C_s	Average number of synaptic contacts between population types	$C_1 = 10$ $C_2 = -560$ $C_3 = 0.6$ $C_4 = 40$ $C_5 = -400$

Appendix D

LaNMM dipole and external stimulation response model

In our framework, we assume that there are two types of dipole generators for a pyramidal neuronal population n depending on the location of the synapse—basal (z_b^n) or apical (z_a^n) dendrites. A dipole, is essentially represented by an orientation (perpendicular to the cortex here), the current induced by a synapse (I) times the separation between the sink and the source,

$$J \sim I \, \Delta z$$

If the synaptic input is apical (with location z_a^n), we assume it has two returns [61]: one in the basal location, and one in the layer just above, each contributing 1/2 of the return needed for current conservation (see equation 2.8 or Fig. 3B)). By superposition (Maxwell's equations are linear), we can think of this as the sum two dipoles, each contributing its own dipole,

$$J_a^n = -\frac{1}{2} I_a^n \left(z_a^n - z_b^n \right) - \frac{1}{2} I_a^n \left(z_a^n - \left(z_b^n + h \right) \right) = I_a^n \left(z_a^n - z_b^n \right) - \frac{1}{2} I_a^n \, h$$

where h is the layer thickness and the signs for each term are due to the sign of the current in the neuron.

Notice that here we have switched from a generic synapse index notation to a more convenient one identifying neuron and apical/basal dendrite, as in $s \sim (n, a/b)$.

If the input is basal (z_b^n), we assume a single return from the layer above, or

$$J_b^n = I_b^n \, h$$

Finally, the total dipole generated by neuron n is the sum of each synpse-return contribution,

$$J^n = I_a^n \, (z_a^n - z_b^n) - \frac{1}{2} I_a^n \, h + I_b^n \, h \tag{D.1}$$

We take the total column dipole to be the sum of pyramidal cell dipoles, i.e., with $J = \sum_n J^n$.

The LaNMM formalism can also be used to represent the effect of an electric field of endogenous (ephaptic) or exogenous (tES, TMS) origin on the membrane potential, adding the term u_E in Equation B.8,

$$v_m(t) = u_E + \sum_s u_s(t) \tag{D.2}$$

$$u_E = \lambda_n \cdot E(t) \tag{D.3}$$

This formulation is called the λE model and it is represented in Fig. 11, see[62].

As a proof of concept, we have simulated the resonance effects of the tACS electric field in the McLaNMM model and have observed that it is displays the expected frequency-amplitude Arnold tongue.

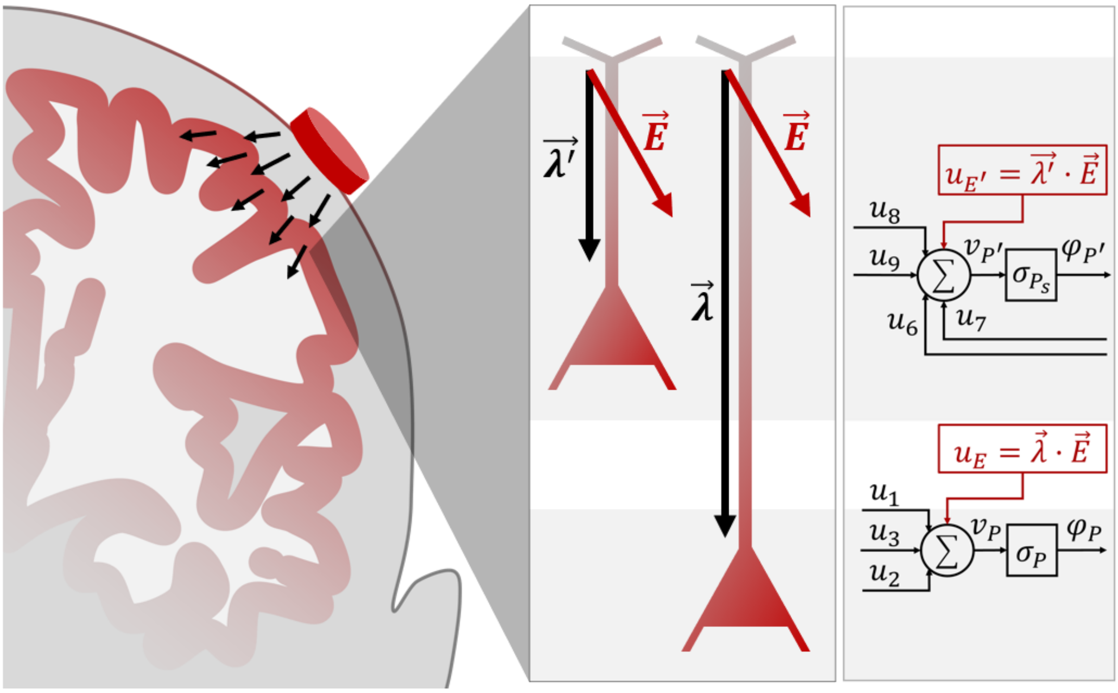

Figure 11: λE model. The pyramidal populations get an extra synapse perturbation proportional to the orientation of the pyramidal population with respect to the external electric field.

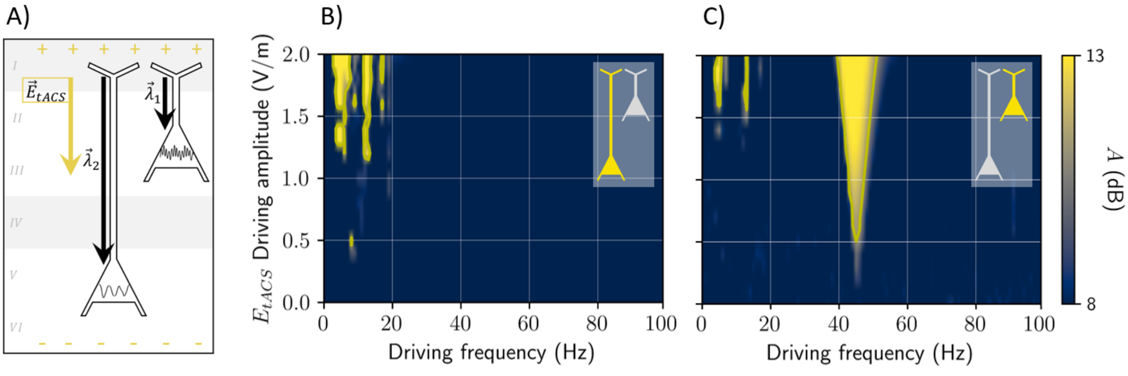

Figure 12: Response to electric field stimulation. A) Schematic representation of the λE model for the McLaNMM. Connectivity between populations and interneurons not shown. B) Membrane potential peak PSD of the deep pyramidal population (Jansen and Rit, oscillating in alpha). C) Superficial population (PING, gamma) depending of the stimulation frequency and amplitude.

Appendix E

Symbols and units

Table 5: Symbols, descriptions and units.

Symbol	**Description**	**Units**
n, m	Neuron index (e.g. P for pyramidal population)	-
s	Synapse index	-
$u_{m\leftarrow n}(t), u_s(t)$	Synaptic membrane potential alteration	mV
$v_n(t)$	Average membrane potential of neuronal population	mV
$\varphi_n(t)$	Average firing rate of neuronal population	Hz
$L_s\big(u_s(t)\big)$	Linear synapse operator	-
C_s	Synapse connectivity constant	-
A_s	Average excitatory/inhibitory synaptic gain	mV
τ_s	Synapse time constant	s^{-1}
$\sigma_m\big(v_m(t)\big)$	Nonlinear operator of a neuronal population	-
e_0	Half of the maximum firing rate	s^{-1}
v_0	Potential when e_0 is achieved	mV
r	Slope of the sigmoid at v_0	mV^{-1}
h	Column layer thickness	m
σ	Tissue conductivity	S/m
z_l, z_l^n	Location along the z axis of each layer ($l \in [1, 6]$). We use z_a for the generic location of apical dendrites and z_b for basal for neuron n.	m
$I_s(z_l)$, I_l^n	Synaptic current induced by synapse s in layer $l \in [a, b]$ of neuron n (positive for current going into cell)	A
η_n	Voltage to current gain factor	A/mV
$R_s(z), R_{s'}(z)$	Distance from source/mirror-source to probe location along z axis	m
$V(z)$	Electric potential	mV
$E_n(z)$	Normal component of the electric field to cortex (positive pointing out of cortex)	V/m
CSD(z)	Current source density (positive as source, i.e., going out of neuron)	A/m^3
J, J^n	Total column dipole density and independent pyramidal cell dipole density J^n (positive pointing out of cortex)	A m/m^3

Appendix F

Additional LFP Data processing

Here we provide additional plots analysing the available macaque data. Figure 13 shows the same metrics as in Figure 4 but with the voltage re-referenced to the first contact. We find that the superficial to superficial PAC and MI coupling disappears. Instead, we observe a positive PAC and MI from deep alpha to deep gamma, which was not find in when the reference was in the PFC chamber. These findings are similar to the ones reported by Ninomiya 2015 (Fig.9), which doesn't find any positive MI between deep alpha oscillations and superficial gamma. No significant AAC was found in this case either.

We computed the same metrics for the bipolar-LFP (Fig.14A) and CSD (Fig.14B). We found, in both cases, a significant PAC and MI from superficial alpha to superficial gamma. Again, no significant AAC was found in either case.

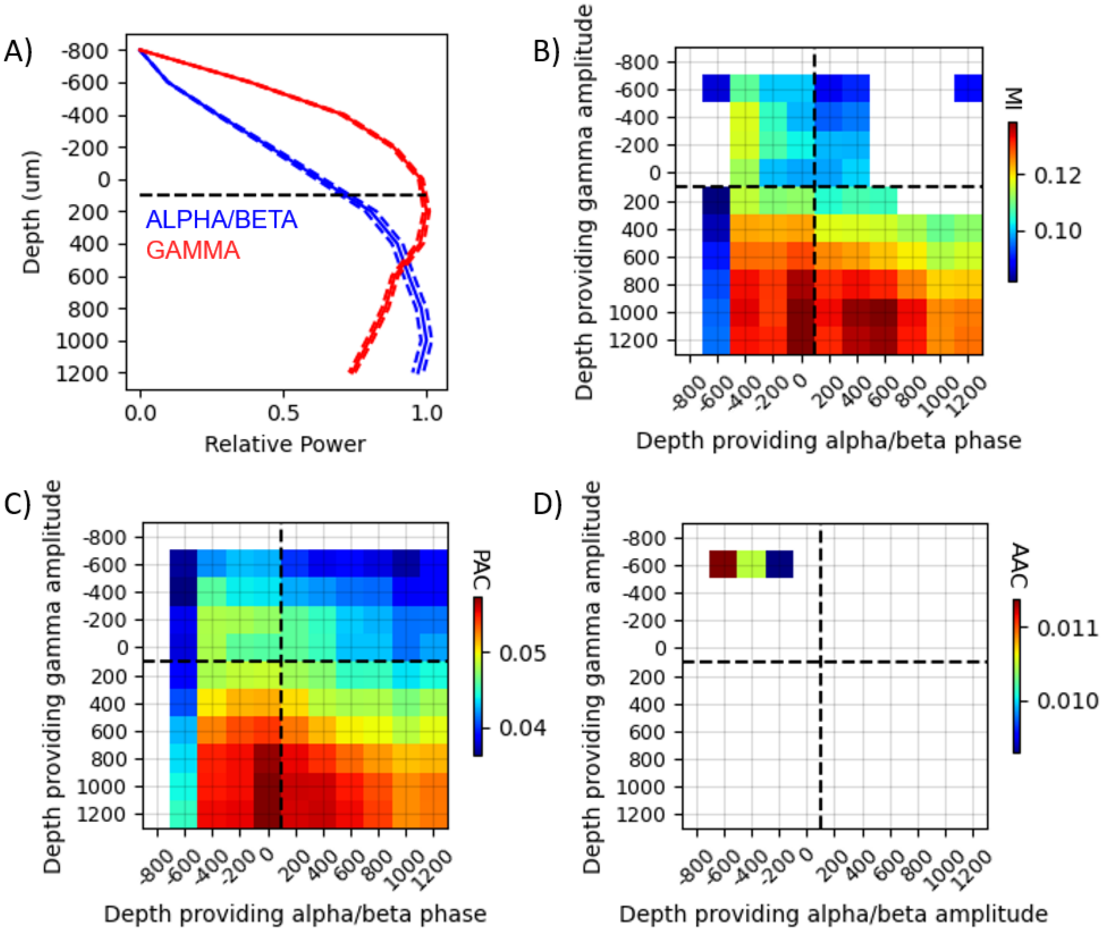

Figure 13: Voltage measures with reference in the first contact. Same metrics and information as in Fig.4

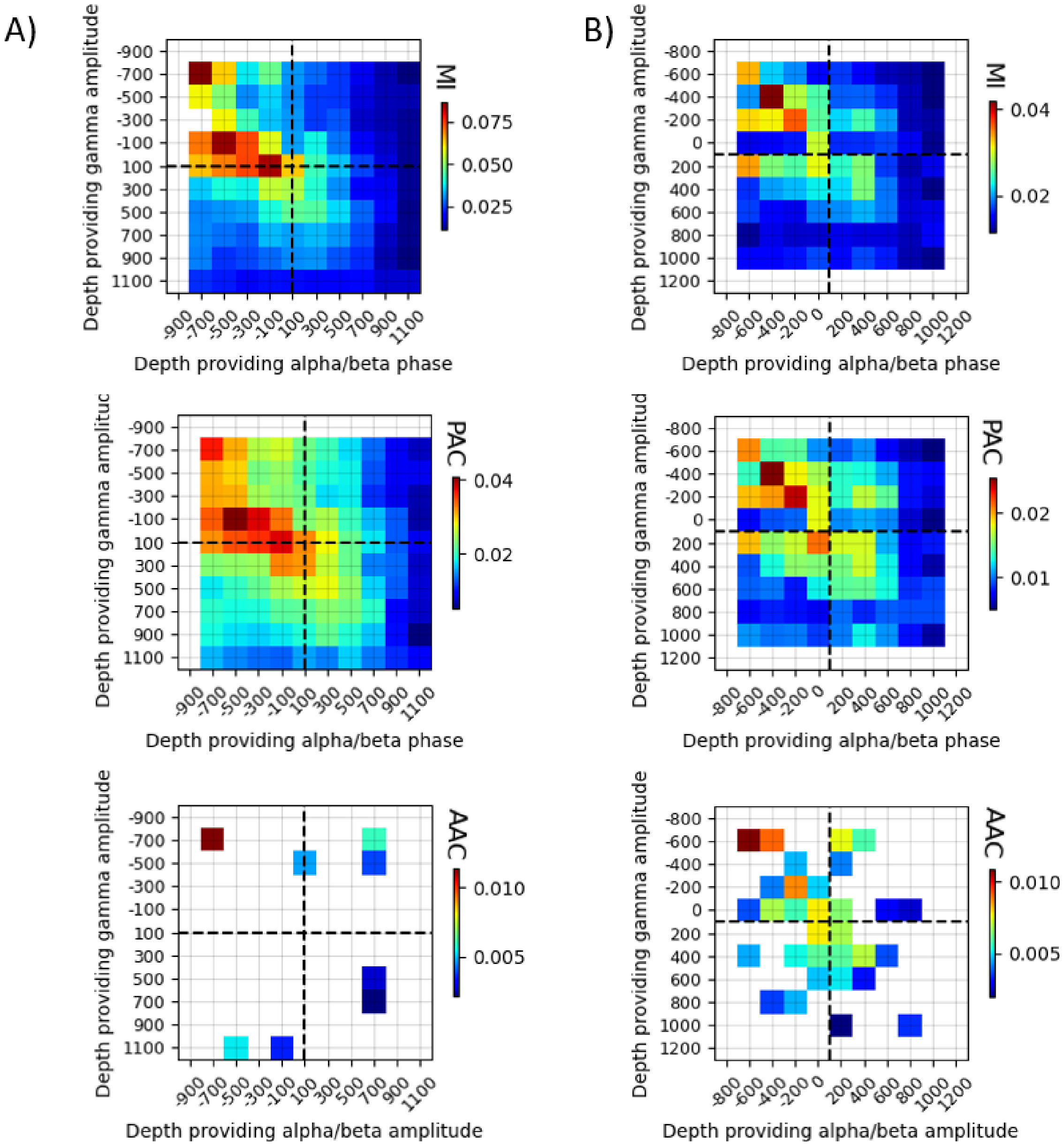

Figure 14: A) nE and B) CSD alpha-gamma coupling profiles.